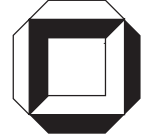


**A constitutive model for
magnetostrictive and piezoelectric materials**

K. Linnemann, S. Klinkel, W. Wagner

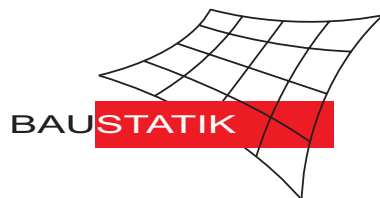
Mitteilung 2(2008)



A constitutive model for magnetostrictive and piezoelectric materials

K. Linnemann, S. Klinkel, W. Wagner

Mitteilung 2(2008)



A constitutive model for magnetostrictive and piezoelectric materials

K. Linnemann^a, S. Klinkel^b, W. Wagner^b

^aFraunhofer Inst. für Kurzzeitdynamik, Ernst-Mach-Institut,
Eckerstraße 4, 79104 Freiburg

^bInstitut für Baustatik, Universität Karlsruhe (TH),
Kaiserstraße 12, 76131 Karlsruhe

Contents

1	Introduction	3
2	Phenomenological behavior	5
2.1	Magnetostrictive materials	6
2.2	Ferroelectric ceramics	8
3	Governing equations	9
3.1	Magnetostriction	9
3.2	Piezoelectricity	11
4	Thermodynamic framework	12
4.1	Integration algorithm	14
4.2	Hardening function	14
5	Algorithmic consistent tangent moduli	15
6	Ferrimagnetic hysteresis effects	16
7	Constitutive modelling of ferroelectric ceramics	17

8 Variational formulation and finite element approximation	17
8.1 Element formulation	18
9 Numerical simulations	20
9.1 Magnetostrictive hysteresis	20
9.2 Ferroelectric hysteresis	22
9.3 Amplified magnetostrictive actuator	23
9.4 Piezoelectric hollow cylinder	27
9.5 Piezoelectric telescope actuator	32
10 Conclusion	33
A Vector notation and linear material constants	35
B Scalar valued conjugated variable to the internal variable	36
C Derivatives for the integration algorithm	36
D Derivatives for the algorithmic consistent tangent moduli	37

Abstract This paper is concerned with a macroscopic nonlinear constitutive law for magnetostrictive alloys and ferroelectric ceramics. It accounts for the hysteresis effects which occur for the considered class of materials. The uniaxial model is thermodynamically motivated and based on the definition of a specific free energy function and a switching criterion. Furthermore, an additive split of the strains and the magnetic or electric field strength into a reversible and an irreversible part is suggested. Analog to plasticity, the irreversible quantities serve as internal variables. A one-to-one-relation between the two internal variables provides conservation of volume for the irreversible strains. The material model is able to approximate the ferromagnetic or ferroelectric hysteresis curves and the related butterfly hysteresis curves. Furthermore, an extended approach for ferrimagnetic behavior which occurs in magnetostrictive materials is presented. A main aspect of the constitutive model is its numerical treatment. The finite element method is employed to solve the coupled field problem. Here the usage of the irreversible field strength permits the application of algorithms of computational inelasticity. The algorithmic consistent tangent moduli are developed in closed form. Hence, quadratic convergence in the iterative solution scheme of governing balance equations is obtained.

Key words Nonlinear constitutive law, magnetostrictive alloys, ferroelectric ceramics, ferromagnetic hysteresis, smart material, computational treatment, finite element method

1 Introduction

Magnetostrictive alloys and ferroelectric ceramics are smart materials. They have a wide range of application for actuation and sensing, see e.g. [Smith \(2005\)](#). Magnetostrictive materials show an inherent coupling between magnetic field and deformation. This effect bears a resemblance to piezoelectricity which describes a coupling between electric field and deformation. Both materials show similar nonlinear behavior. The purpose of this paper is the development of a constitutive model which accounts for the nonlinear behavior and hysteresis effects of magnetostrictive alloys and ferroelectric ceramics.

Microscopically motivated models approximate the switching processes for each single crystallite. The process is modeled by an energy criterion. The macroscopic behavior is obtained by averaging over a large number of union cells. Microscopically motivated models for ferroelectric ceramics are presented in e.g. [Chen and Lynch \(2001\)](#), [Hwang et al. \(1995, 1998\)](#) and [Huber and Fleck \(2001\)](#). Approaches for magnetostrictive materials are often based on the model of [Jiles and Atherton \(1986\)](#) which was primarily developed for ferromagnetic hysteresis without magnetoelastic coupling. The formulation approximates the bending and movement of the domain walls during the magnetization. Extended models for magnetostrictive material are found in e.g. [Sablik and Jiles \(1993\)](#), [Jiles \(1995\)](#), [Calkins et al. \(2000\)](#), [Dapino et al. \(2000b\)](#), [Dapino et al. \(2000a\)](#), and [Dapino et al. \(2002\)](#). With the consideration of switching for each crystallite microscopically motivated models generally lead to a large number of internal variables which increases the numerical effort.

Macroscopical constitutive models are based on a phenomenological description of the material behavior. This reduces the amount of internal variables. A widespread approach is the model of [Preisach \(1935\)](#) which was originally developed to describe the magnetization of ferromagnetics. The choice of parameters allows the simulation of a wide range of hysteresis curves. Formulations for magnetostrictive alloys are proposed in [Adly et al. \(1991\)](#) and [Tan and Baras \(2004\)](#). Applications of the Preisach model for piezoelectric hysteresis are published in [Hwang et al. \(1995\)](#), [Pasco and Berry \(2004\)](#), [Yu et al. \(2002a,b\)](#) and [Butz et al. \(2005, 2008\)](#). The Preisach model is purely phenomenological and not thermodynamically consistent.

Another class of constitutive models are formulated in accordance with the principles of thermodynamics. The material behavior is determined with the definition of a specific free energy function. For piezoelectric ceramics the strains, the polarization, and the temperature often serve as independent variables. For magnetostrictives the magnetization is used instead of the polarization. Here, a common approach are higher order energy functions, see e.g. [Carman and Mitrovic \(1995\)](#), [Wan et al. \(2003\)](#), [Zheng and Liu \(2005\)](#), and [Zheng and Sun \(2007\)](#). Alternatively a definition of the free energy function in sections is used, see [Wan et al. \(2003\)](#) and [Smith et al. \(2003\)](#). The independent variables are splitted in a reversible and an irreversible part for the approx-

imation of the hysteresis behavior. The irreversible quantities serve as internal variables and represent the polarization or magnetization state. The development of the internal variables is determined with the definition of a switching criterion. The model of Fang et al. (2004) for magnetostrictive materials is based on these assumptions. More often, thermodynamically motivated models are applied for piezoelectric ceramics. The approaches of Kamlah (2001), Kamlah and Böhle (2001) and Elhadrouz et al. (2005) use multiple switching criterions to specify begin and end of the irreversible behavior. The multiaxial models of Landis (2002) and McMeeking and Landis (2002) get along with only one switching criterion. The domain processes are restricted by a hardening functions. Schröder and Gross (2004) and Schröder and Romanowski (2005) present a co-ordinate invariant formulation on this assumption. The models of McMeeking and Landis (2002), Kamlah (2001), Schröder and Romanowski (2005) use a one to one relation between irreversible strains and polarization to ensure that domain switching induces irreversible strains. This assumption is sufficient for electrical loading but prevents the simulation of ferroelastic behavior or mechanical depolarization. The circumvent this disadvantage Kamlah (2001) decomposes the irreversible strains in a part for ferroelectric and one for ferroelastic switching processes. A more general approach is published in Landis (2002) and Klinkel (2006a,b). Here a coupled switching criterions and hardening functions are used to control the change of the irreversible strains. Mehling et al. (2007) introduce an orientation distribution function as additional internal variable to approximate coupled electromechanical loadings.

In the present paper a thermodynamic motivated constitutive model is developed which accounts for hysteresis effects in ferroelectric ceramics and magnetostrictive alloys. The uniaxial model is embedded in a three dimensional formulation. This benefits an efficient numerical treatment of the model but prevents a reorientation of magnetization or polarization during the simulation. The electric respectively the magnetic field strength is splitted additively. The irreversible field strength serves with the irreversible strains as internal variable. The main aspects of the model may be summarized as follows:

- A thermodynamically consistent constitutive model is presented. The formulation is based on the definition of a free energy function and a switching criterion. A polynomial of second order is used as free energy function. The switching criterion controls domain switching. The center of the switching surface moves in the sense of kinematic hardening in plasticity.
- The strains, the magnetic and the electric field strength respectively are decomposed additively in a reversible and an irreversible part. The split of the field strength is an alternative approach to the decomposition of the magnetization or polarization. Its application is motivated by the

numerical treatment of the constitutive model with the finite element method. Here the field strength is described with a scalar potential which serves as nodal degrees of freedom. So no change of variables is necessary. Furthermore, one may draw on algorithms of computational inelasticity.

- A one to one relation between the irreversible quantities is utilized to maintain volume conservation during the irreversible processes. A hardening function restricts the growth of the internal variable near saturation.
- The model is able to reproduce the ferroelectric and butterfly hysteresis of ferroelectric ceramics. Furthermore, the typical hysteresis of magnetostrictive alloys can be simulated. The occurring ferrimagnetic hysteresis behavior of these materials is approximated by an expanded approach which is based on a transformation of the independent variables in a local description. Ferroelastic switching and mechanical depolarization are not considered within this work.
- For the numerical treatment of the problem the finite element method is employed. The constitutive model is implemented in a hexahedral element. Therefore the evolution equation is integrated by an implicit Euler backward algorithm which leads to a local iteration. The algorithmic consistent tangent moduli are formulated in closed form. Accordingly, quadratic convergence in the iterative Newton-Raphson solution scheme is guaranteed.

The outline of the paper is as follows: Section 2 deals with the phenomenological behavior of magnetostrictive and piezoelectric materials. In Section 3 the governing equations of the coupled field problems are introduced. The thermodynamic framework of the constitutive model is presented in Section 4. In Section 5 the algorithmic consistent tangent moduli are developed. An expanded model for ferrimagnetic behavior is presented in Section 6. Section 7 deals with the modeling of ferroelectric ceramics. In Section 8 the variational formulation and the finite element approximation are presented. The numerical examples in Section 9 show the capabilities and main characteristics of the proposed constitutive model.

2 Phenomenological behavior

This section summarizes the behavior of the considered smart materials. At first we account for the origin and phenomenology of magnetostriction. For extended treatises on magnetism of solids, the books of [Bozorth \(1964\)](#) and [Engdahl \(2000\)](#) are recommended. The second part of the section is concerned with piezoelectric coupling, in particular with ferroelectric ceramics. It briefly

deals with the differences to the magnetostrictive model. Piezoelectricity is well documented in literature, see Jaffe et al. (1971) and Ikeda (1990). A good survey of the basic phenomenons of ferroelectric ceramics and their nonlinear effects is given in e.g. Kamlah (2001).

2.1 Magnetostriuctive materials

The term magnetostriction is applied for several magneto-elastic coupling phenomena. The most utilized effect is the Joule magnetostriction which denotes a deformation of a specimen due to an applied magnetic field \vec{H} . The reciprocal Villari effect is characterized by a change of the magnetization \vec{M} induced by a mechanical deformation. Both phenomena occur in all ferro-, ferri, and antiferromagnetic materials. The magnetic properties of these materials originate from magnetic moments \vec{m} which results from the spins of electrons in uncomplete occupied inner orbitals of the atom. Due to spin orbit coupling, which is a purely quantum mechanical interaction, the magnetic moments are closely connected with the shape of the electron hull $-e$. The electrical negative electron hull effects Coulomb forces to the neighboring atoms in the lattice. Regarding the complex shape of $-e$ these forces are not isotropic, which is important for magnetostrictive coupling. This correlation is described by means of a sample crystallite depicted in Fig. 1. Above the Curie temperature T_c the magnetic moments are disordered, see Fig. 1a). Cooling the material down below T_c , the exchange interaction causes a parallel ordering of the atoms in the lattice, see Fig. 1b). Applying an external magnetic field the magnetic moments switch in the direction of \vec{H} . This process is associated with the rotation of the electron hulls $-e$. Along with the rotation of $-e$ the Coulomb forces between the atoms change and the gaps in the lattice shift. Consequently, a deformation of the specimen is observed, see Fig. 1c). The magnetostrictive strains are denoted by λ_{\parallel} and λ_{\perp} . The volume conservation of the deformation involves $\lambda_{\perp} = -\frac{1}{2}\lambda_{\parallel}$. Depending on the electron configuration some materials show a positive magnetostriction with $\lambda_{\parallel} > 0$. For materials with negative magnetostriction it holds $\lambda_{\parallel} < 0$.

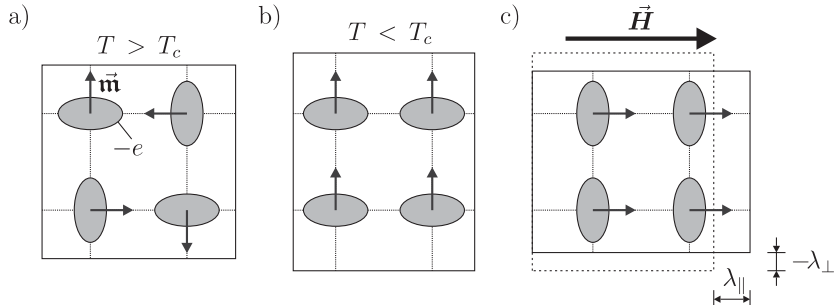


Figure 1: Illustration of the Joule magnetostriction

To illustrate the origin of the Villari Effect a crystallite with positive mag-

netostriction below T_c is considered, see Fig. 2a). The sample is deformed by a mechanical stress \mathbf{S} parallel to $\vec{\mathbf{m}}$. The deformation shifts the inter-atomic distances in the lattice. This change makes sure that another direction of the magnetic moments is energetically convenient. So the magnetic moments rotate as depicted in Fig. 2b). Since no direction of the magnetic moments is specified by \mathbf{S} , the orientations of Fig. 2b) and c) have the same probability. This results generally in a reduction of the magnetization for polycrystalline materials.

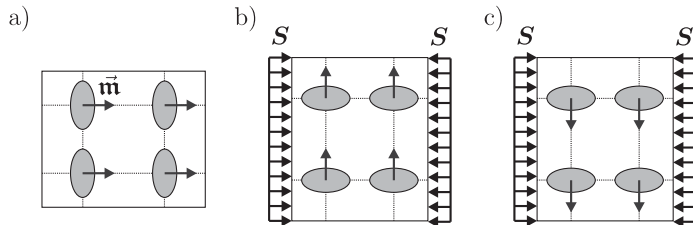


Figure 2: Illustration of the Villari effect

Parallel aligned magnetic moments are energetically not favorable on mesoscopic scale. Hence, the crystallites are divided in substructures, the so-called domains. The magnetic moments in each domain are aligned parallel, which is caused by the exchange interaction. The neighboring domains have an opposite magnetization direction to minimize the magnetic energy. They are separated by domain walls. The structure of a polycrystalline material is shown in Fig. 3.

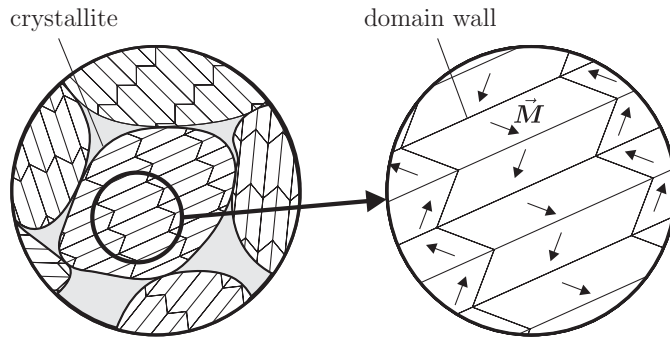


Figure 3: Domain structure of a magnetostrictive alloy

The nonlinear behavior of magnetostrictive materials is strongly connected with the domain structure. If a magnetic field is applied to a specimen, the magnetic moments along the domain walls begin to rotate in the direction of $\vec{\mathbf{H}}$. The domain walls begin to move. Due to discontinuities in the lattice the movements of the domain walls are irreversible processes. Hence, for an oscillating magnetic field hysteresis curves are observed. In the ferromagnetic hysteresis curve the magnetic flux density $\vec{\mathbf{B}}$ is plotted versus the field strength $\vec{\mathbf{H}}$. The curve of Fig. 4a) is exemplary plotted for the X_1 direction. The

ordinate of the so called butterfly hysteresis in Fig. 4b) is the strain component E_{11} . The domain states are sketched for both figures. The characteristic values of the curves are the coercive field strength \vec{H}_c and the remanent values \vec{B}_{rem} and E_{rem} .

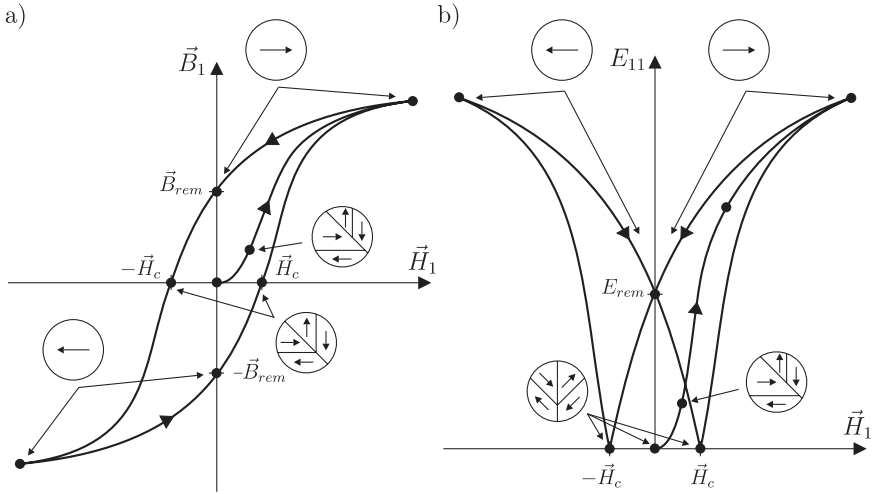


Figure 4: Ferromagnetic and butterfly hysteresis curves in magnetostrictive materials

Commercial available magnetostrictive alloys like Terfenol-D show a ferri-magnetic behavior which is affected by mechanical prestress. The ferrimagnetic lattice consists of two interleaving lattices with contrary magnetization. For an applied magnetic field \vec{H} one of these lattices switches in the direction of \vec{H} , the other one remains unchanged. In the absence of mechanical loading both lattices are switching. The specimen behaves like a ferromagnetic material. For mechanical prestress this switching process is hampered. As a result the characteristic hysteresis curves are separated in respectively two hysteresis as shown in Fig. 5.

2.2 Ferroelectric ceramics

The basic attribute of ferroelectric ceramics is the polarization, analog to the magnetization in ferromagnetics. Below T_c the centers of positive and negative charges are situated at different locations in the unit cell, which results in a spontaneous polarization. The direction of the polarization can be changed by applying an electrical or mechanical loading. Due to the Coulomb forces, the central metal ion shifts within the unit cell which causes a distortion. Similar to ferromagnetism the direction of the polarization is aligned parallel on microscopic level. On the mesoscopic scale a domain structure evolves to minimize the electrostatic energy. Again, the nonlinear behavior of the material is affected by switching processes along the domain walls resulting in wall movements. The observed hysteresis curves are very similar to the

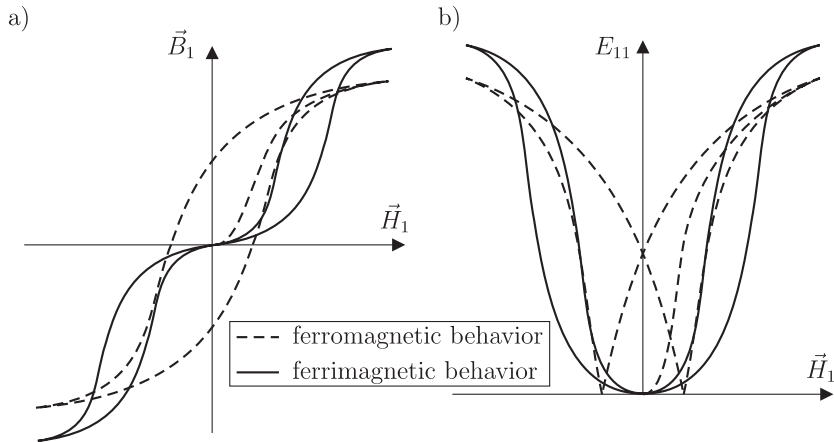


Figure 5: Ferromagnetic and butterfly hysteresis curves in magnetostrictive materials

ones of magnetostrictive materials. Additionally, for a mechanical load cycle a so called ferroelastic hysteresis can be measured which does not occur in magnetostrictives. Ferroelastic hysteresis effects are not considered in this paper.

3 Governing equations

In this section the governing equations of magnetostrictive and piezoelectric materials are described. Again the first part is addicted to magnetostrictives. The annotations to piezoelectricity are summarized briefly with respect to differences and similarities to the magnetoelastic coupling.

3.1 Magnetostriiction

The balance equations of magnetostrictive coupled problems are the strong form of equilibrium and the Maxwell equation considering solenoidality of the magnetic field. The local forms are given as

$$\mathbf{S} \nabla + \rho \mathbf{b} = \mathbf{0} \quad (1)$$

$$\vec{\mathbf{B}} \cdot \nabla = 0. \quad (2)$$

Here, \mathbf{S} stands for the stress tensor, $\rho \mathbf{b}$ for the mechanical body forces and $\vec{\mathbf{B}}$ for the magnetic flux density. Thus the influence of ponderomotive forces is minor, they are neglected in this paper. In consequence the stress tensor is symmetric. The mechanical and magnetic boundary conditions read

$$\mathbf{S} \cdot \mathbf{n} = \mathbf{t} \quad \text{on } \partial_t \mathcal{B}_0 \quad (3)$$

$$\vec{\mathbf{B}} \cdot \mathbf{n} = \varsigma_M \quad \text{on } \partial_s \mathcal{B}_0. \quad (4)$$

The vector \mathbf{t} denotes the prescribed traction on the surface $\partial_t \mathcal{B}_0$ and the scalar value ς_M the magnetic surface charge on $\partial_s \mathcal{B}_0$. ς_M is an imaginary quantity, because of magnetic monopoles do not exist. But its introduction is beneficial if the magnetic scalar potential is used, see also the examples in section 9. The vector \mathbf{n} gives the outward unit normal on $\partial \mathcal{B}_0$. The linear strain tensor \mathbf{E} and the magnetic field strength $\vec{\mathbf{H}}$ are defined as

$$\mathbf{E} = \frac{1}{2}(\nabla \otimes \mathbf{u} + \mathbf{u} \otimes \nabla) \quad (5)$$

$$\vec{\mathbf{H}} = -\nabla \phi_M, \quad (6)$$

where \mathbf{u} is the displacement vector and ϕ_M the magnetic scalar potential. The scalar potential is used instead of the magnetic vector potential, because only fields without curl are considered. For the constitutive model the total strains and the magnetic field strength are decomposed additively as

$$\mathbf{E} = \mathbf{E}^r + \mathbf{E}^i \quad (7)$$

$$\vec{\mathbf{H}} = \vec{\mathbf{H}}^r + \vec{\mathbf{H}}^i. \quad (8)$$

The superscript r denotes the reversible part. The irreversible quantities, indexed by i , serve as internal variables and describe the dissipative part. Eq. (7) is in full accordance with small strain plasticity theory. The additive split of field strength is a novel aspect of the proposed model. More common is a decomposition of the magnetization, see Fang et al. (2004), or the split of the polarization for piezoelectric models, see e.g. McMeeking and Landis (2002), Kamlah (2001), Schröder and Romanowski (2005). The additive split of the magnetic field is an alternative approach to describe the remanent changes of the magnetization. It is not motivated physically but by the numerical treatment of the constitutive model. The analogy to plasticity permits the usage of soloing algorithms of computational inelasticity. Furthermore a Legendre transformation of the constitutive equations is not necessary for the finite element formulation. Fig. 6 illustrates $\vec{\mathbf{H}}^i$ in an idealized ferromagnetic hysteresis curve. For a magnetic field lower \vec{H}_c linear behavior is assumed. Accordingly, $\|\vec{\mathbf{B}}\| < \vec{M}_c$ with $\vec{M}_c = \vec{H}_c \mu$ is applied for the magnetic flux density. For field strengths higher than \vec{H}_c irreversible wall movements are presumed which are associated with a change of the internal variable $\vec{\mathbf{H}}^i$. For the fully magnetized material reversible behavior is assumed. The growth of $\vec{\mathbf{H}}^i$ stopped if its norm is equal to \vec{H}_s^i . The saturation value \vec{H}_s^i is estimated from \vec{B}_{rem} . Generally the hysteresis is curved. Here the permeability μ , which is described by the gradient of the tangent, depends on the chosen working point. In the following μ is defined for $\|\vec{\mathbf{H}}\| = 0$ and $\|\vec{\mathbf{B}}\| = \vec{B}_{rem}$. Accordingly $\vec{H}_s^i = \vec{B}_{rem}/\mu$ is also valid for the general case.

Due to conservation of volume, which is claimed for the irreversible strains, a one-to-one relation is assumed as

$$\mathbf{E}^i = \frac{E_s}{(\vec{H}_s^i)^2} \vec{\mathbf{H}}^i \cdot \vec{\mathbf{H}}^i \mathbf{I}. \quad (9)$$

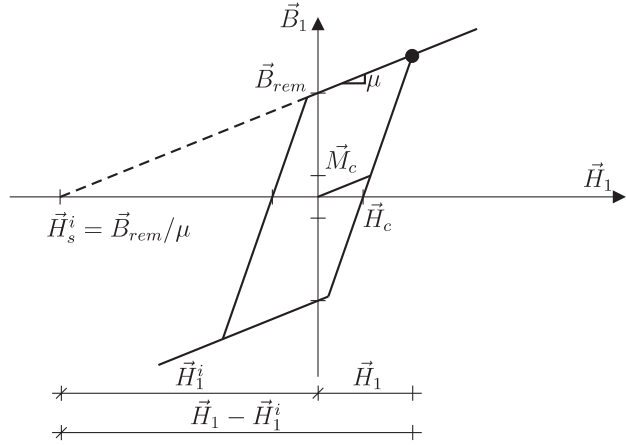


Figure 6: Idealized ferromagnetic hysteresis

this is similar to ferroelectric models where this ansatz is common, see e.g. Kamlah (2001), McMeeking and Landis (2002). The one to one relation links the irreversible strains and field strength. This reduces the amount of internal variables to the vector \vec{H}^i . But Eq. (9) is only valid for pure electrical loadings. Ferroelastic behavior or mechanical depolarization is not approximated with this approach. The quantity \mathbf{I} denotes the projection tensor of rank two given as

$$\mathbf{I} = \frac{3}{2} \left(\mathbf{e} \otimes \mathbf{e} - \frac{1}{3} \mathbf{1} \right) \quad \text{with} \quad \mathbf{e} = \frac{\vec{H}^i}{\|\vec{H}^i\|}. \quad (10)$$

The magnetization arises along a given direction \mathbf{e} . The formulation is restricted to an uniaxial constitutive model with this assumption. A reorientation of the magnetization direction \mathbf{e} is not possible yet. But the approach permits a more efficient computational treatment of the model, see Sec. 5

3.2 Piezoelectricity

The balance equations of the piezoelectric coupled problem are given by Eq. (1) and the local form of the Gauss' law

$$\vec{D} \cdot \nabla = 0 \quad (11)$$

instead of Eq. (2). The vector \vec{D} stands for the dielectric displacements. In case of dielectrics free volume charges are not considered. The boundary conditions are given in Eq. (3) and supplemented with

$$\vec{D} \cdot \mathbf{n} = \varsigma_E \quad \text{on } \partial_s \mathcal{B}_0, \quad (12)$$

where ς_E is the electric surface charge. The electric field \vec{E} is described via

$$\vec{E} = -\nabla \phi_E \quad (13)$$

with the electric scalar potential ϕ_E . Similar to Klinkel (2006a) the total electric field is additively decomposed as

$$\vec{E} = \vec{E}^r + \vec{E}^i, \quad (14)$$

where \vec{E}^i is the irreversible electric field. It serves as internal variable and replaces \vec{H}^i in Eq. (9). Additionally the saturation parameter \vec{E}_s^i is applied instead of \vec{H}_s^i and \vec{P}_c instead of \vec{M}_c . The similarities of magnetomechanical and electromechanical coupling are obvious. Further the formulation is exclusively formulated for magnetostrictive problems.

4 Thermodynamic framework

The constitutive model is based on a free energy function which serves as thermodynamic potential

$$\begin{aligned} \rho\psi = & \frac{1}{2}(\mathbf{E} - \mathbf{E}^i) : \mathbb{C} : (\mathbf{E} - \mathbf{E}^i) + \frac{\vec{H}^i \cdot \mathbf{e}}{\vec{H}_s^i} (\mathbf{E} - \mathbf{E}^i) : \mathbf{e} \cdot \vec{H} \\ & - \frac{1}{2}(\vec{H} - \vec{H}^i) \cdot \boldsymbol{\mu} (\vec{H} - \vec{H}^i) + \rho\bar{\psi}(\vec{H}^i). \end{aligned} \quad (15)$$

Here, \mathbb{C} , \mathbf{e} , and $\boldsymbol{\mu}$ are elasticity tensor, piezomagnetic coupling tensor and permeability. In the present work a second order potential is used. Thus Eq. (15) is quadratic in \mathbf{E} und \vec{H} . The last term $\rho\bar{\psi}(\vec{H}^i)$ represents the energy stored in the internal variable \vec{H}^i . With respect to plasticity it is called hardening function. According to the second law of thermodynamics and with neglecting thermal effects the Clausius-Duhem inequality reads

$$\mathcal{D} = \mathbf{S} : \dot{\mathbf{E}} - \vec{B} \cdot \dot{\vec{H}} - \rho\dot{\psi} \geq 0 \quad (16)$$

The scalar \mathcal{D} names the dissipated energy. Using standard arguments of rational continuum mechanics, see Coleman and Noll (1963), the stress and the magnetic flux density can be derived as

$$\mathbf{S} := \frac{\partial \rho\psi}{\partial \mathbf{E}} = \mathbb{C} : (\mathbf{E} - \mathbf{E}^i) + \frac{\vec{H}^i \cdot \mathbf{e}}{\vec{H}_s^i} \mathbf{e} \cdot \vec{H} \quad (17)$$

$$-\vec{B} := \frac{\partial \rho\psi}{\partial \vec{H}} = \frac{\vec{H}^i \cdot \mathbf{e}}{\vec{H}_s^i} \mathbf{e}^T : (\mathbf{E} - \mathbf{E}^i) - \boldsymbol{\mu} (\vec{H} - \vec{H}^i). \quad (18)$$

Applying this definitions and the derivation in time of Eq. (9) the dissipation reduces to

$$\mathcal{D} = - \underbrace{\left(2 \frac{E_s}{(\vec{H}_s^i)^2} \frac{\partial \rho\psi}{\partial \mathbf{E}^i} : \mathbf{I} \vec{H}^i + \frac{\partial \rho\psi}{\partial \vec{H}^i} \right)}_{\Xi} \cdot \dot{\vec{H}}^i \geq 0, \quad (19)$$

in which $\boldsymbol{\Xi}$ is defined as the work conjugated variable to the internal variable $\vec{\mathbf{H}}^i$. The partial derivatives are given by

$$\frac{\partial \rho\psi}{\partial \mathbf{E}^i} = \mathbf{S} \quad (20)$$

$$\frac{\partial \rho\psi}{\partial \vec{\mathbf{H}}^i} = \frac{1}{\vec{H}_s^i} \left[(\mathbf{E} - \mathbf{E}^i) : \mathbf{e} \cdot \vec{\mathbf{H}} \right] \mathbf{e} - \boldsymbol{\mu} (\vec{\mathbf{H}} - \vec{\mathbf{H}}^i) - \frac{\partial \rho\bar{\psi}}{\partial \vec{\mathbf{H}}^i}. \quad (21)$$

A switching criterion is introduced to signify the begin of irreversible domain processes

$$\Phi = \frac{\boldsymbol{\Xi} \cdot \boldsymbol{\Xi}}{\vec{M}_c^2} - 1 \leq 0. \quad (22)$$

Here the parameter \vec{M}_c serves as coercive value. Reversible wall movements in the domains are assumed for $\Phi < 0$. For irreversible wall movements it holds $\Phi = 0$. The postulate of maximum dissipation is formulated by a Lagrange functional with Φ as constraint. It reads

$$\mathcal{L} = -\mathcal{D}(\boldsymbol{\Xi}) + \lambda \Phi(\boldsymbol{\Xi}), \quad (23)$$

where λ is the Lagrange multiplier. The solution of Eq. (23) requires

$$\frac{\partial \mathcal{L}}{\partial \boldsymbol{\Xi}} = 0 \quad \text{and} \quad \frac{\partial \mathcal{L}}{\partial \lambda} = \Phi(\boldsymbol{\Xi}) = 0. \quad (24)$$

The necessary conditions for the existence of a local minimum are given by the Kuhn-Tucker conditions

$$\lambda \geq 0, \quad \Phi \leq 0, \quad \lambda \Phi = 0. \quad (25)$$

The evolution equation for the internal variable $\vec{\mathbf{H}}^i$ is derived from Eq. (24)₁

$$\dot{\vec{\mathbf{H}}}^i = 2 \lambda \frac{\boldsymbol{\Xi}}{\vec{M}_c^2}. \quad (26)$$

It gives the rate of $\vec{\mathbf{H}}^i$ for a given \mathbf{E} and $\vec{\mathbf{H}}$. Eq.(19) implies that $\vec{\mathbf{H}}^i$ is parallel to \mathbf{e} a scalar valued internal variable $\alpha = (\vec{\mathbf{H}}^i \cdot \mathbf{e})/\vec{H}_s^i$ is introduced. Furthermore, its work conjugated variable is reduced to the scalar $\bar{\Xi}$ with $\boldsymbol{\Xi} = \bar{\Xi} \mathbf{e}$ which is given in Appendix B. The governing equations for the optimization problem read

$$\dot{\alpha} = 2 \lambda \frac{\bar{\Xi}}{\vec{M}_c^2} \quad (27)$$

$$\Phi = \frac{\bar{\Xi}^2}{\vec{M}_c^2} - 1 = 0. \quad (28)$$

4.1 Integration algorithm

The evolution equation (27) is integrated in time. Here the implicit Euler scheme is used, because it is unconditionally stable. The time t is discretized in time steps. It is assumed that all values for the time step t_n are known. The internal variable α_{n+1} at $t_{n+1} = t_n + \Delta t$ has to be determined for an incremental $\Delta \mathbf{E}$ or $\Delta \vec{\mathbf{H}}$. The discrete form of Eq. (27) in the interval $[t_n, t_{n+1}]$ read

$$\alpha_{n+1} = \alpha_n + 2 \gamma \frac{\bar{\Xi}_{n+1}}{\vec{M}_c^2} \quad (29)$$

with $\gamma = \lambda(t_{n+1} - t_n)$. For irreversible processes it holds $\Phi_{n+1} = 0$. The switching criterion depends on the conjugated variable $\bar{\Xi}_{n+1}$ which is a function of the unknown α_{n+1} . For the first predictor step a trial value $\alpha_{trial} = \alpha_n$ is assumed. If the switching criterion is satisfied with the trial value, α_{trial} is equal to α_{n+1} . If not, a radial return algorithm with the following residua is applied

$$\begin{aligned} R_a &= \alpha_{n+1} - \alpha_n - 2 \gamma \frac{\bar{\Xi}_{n+1}}{\vec{M}_c^2} = 0 \\ R_b &= \frac{\bar{\Xi}_{n+1}^2}{\vec{M}_c^2} - 1 = 0. \end{aligned} \quad (30)$$

These equations are iteratively solved by a local Newton iteration

$$\begin{aligned} \frac{\partial R_a^{(k)}}{\partial \alpha_{n+1}} \Delta \alpha + \frac{\partial R_a^{(k)}}{\partial \gamma} \Delta \gamma &= -R_a^{(k)} \\ \frac{\partial R_b^{(k)}}{\partial \alpha_{n+1}} \Delta \alpha + \frac{\partial R_b^{(k)}}{\partial \gamma} \Delta \gamma &= -R_b^{(k)} \end{aligned} \quad (31)$$

with

$$\begin{aligned} \alpha_{n+1}^{(k+1)} &= \alpha_{n+1}^{(k)} + \Delta \alpha \\ \gamma^{(k+1)} &= \gamma^{(k)} + \Delta \gamma. \end{aligned} \quad (32)$$

The iteration step is denoted by the superscript (k) . The partial derivatives needed in Eq.(31) are given in Appendix C.

4.2 Hardening function

The hardening function $\rho \bar{\psi}$ determines the shape of the ferromagnetic and butterfly hysteresis curves. It is defined as

$$\frac{\partial \rho \bar{\psi}}{\partial \vec{\mathbf{H}}^i} := \left[k \vec{H}_s^i \alpha + a \operatorname{arctanh} \left(\frac{\alpha}{b} \right) \right] \mathbf{e} \quad (33)$$

with the material parameters k , a , and b . The first summand means linear hardening. The second one restricts the growth of α near saturation.

5 Algorithmic consistent tangent moduli

The numerical solution of the boundary value problem requires an iterative method for nonlinear constitutive models. To obtain quadratic convergence the Newton-Raphson iteration scheme is applied. Here, consistent linearizations of \mathbf{S} and $\vec{\mathbf{B}}$ are needed for the load step t_{n+1} . It reads

$$d\mathbf{S}_{n+1} = \tilde{\mathbb{C}}_{n+1} : d\mathbf{E}_{n+1} + \tilde{\mathbf{e}}_{n+1} \cdot d\vec{\mathbf{H}}_{n+1} \quad (34)$$

$$d\vec{\mathbf{B}}_{n+1} = \tilde{\mathbf{e}}_{n+1} : d\mathbf{E}_{n+1} + \tilde{\boldsymbol{\mu}}_{n+1} d\vec{\mathbf{H}}_{n+1}. \quad (35)$$

The tangent moduli $\tilde{\mathbb{C}}$, $\tilde{\mathbf{e}}_{n+1}$ and $\tilde{\boldsymbol{\mu}}_{n+1}$ can be employed by numerical evaluation. A more efficient formulation is obtained by deriving them in closed form. The total derivatives of \mathbf{S}_{n+1} and $\vec{\mathbf{B}}_{n+1}$ are given by

$$d\mathbf{S}_{n+1} = \left| \frac{\partial \mathbf{S}}{\partial \mathbf{E}} : d\mathbf{E} + \frac{\partial \mathbf{S}}{\partial \vec{\mathbf{H}}} d\vec{\mathbf{H}} + \frac{\partial \mathbf{S}}{\partial \alpha} d\alpha \right|_{n+1} \quad (36)$$

$$d\vec{\mathbf{B}}_{n+1} = \left| \frac{\partial \vec{\mathbf{B}}}{\partial \mathbf{E}} : d\mathbf{E} + \frac{\partial \vec{\mathbf{B}}}{\partial \vec{\mathbf{H}}} d\vec{\mathbf{H}} + \frac{\partial \vec{\mathbf{B}}}{\partial \alpha} d\alpha \right|_{n+1}. \quad (37)$$

Terms depending on the internal variable α_{n+1} have to be eliminated. The consistency condition $\dot{\Phi}\lambda = 0$ implies $d\Phi_{n+1} = 0$ for irreversible processes. Consequently $d\bar{\Xi}_{n+1} = 0$ gives an equation for $d\alpha_{n+1}$. It reads

$$d\alpha_{n+1} = \left| - \left[\frac{\partial \bar{\Xi}}{\partial \mathbf{E}} : d\mathbf{E} + \frac{\partial \bar{\Xi}}{\partial \vec{\mathbf{H}}} \cdot d\vec{\mathbf{H}} \right] \frac{1}{\frac{\partial \bar{\Xi}}{\partial \alpha}} \right|_{n+1}. \quad (38)$$

With substituting Eq. (38) in Eqs. (36) and (37) one obtains

$$d\mathbf{S}_{n+1} = \left| \left[\frac{\partial \mathbf{S}}{\partial \mathbf{E}} - \frac{1}{\frac{\partial \bar{\Xi}}{\partial \alpha}} \frac{\partial \mathbf{S}}{\partial \alpha} \otimes \frac{\partial \bar{\Xi}}{\partial \mathbf{E}} \right] : d\mathbf{E} + \left[\frac{\partial \mathbf{S}}{\partial \vec{\mathbf{H}}} - \frac{1}{\frac{\partial \bar{\Xi}}{\partial \alpha}} \frac{\partial \mathbf{S}}{\partial \alpha} \otimes \frac{\partial \bar{\Xi}}{\partial \vec{\mathbf{H}}} \right] \cdot d\vec{\mathbf{H}} \right|_{n+1} \quad (39)$$

$$d\vec{\mathbf{B}}_{n+1} = \left| \left[\frac{\partial \vec{\mathbf{B}}}{\partial \mathbf{E}} - \frac{1}{\frac{\partial \bar{\Xi}}{\partial \alpha}} \frac{\partial \vec{\mathbf{B}}}{\partial \alpha} \otimes \frac{\partial \bar{\Xi}}{\partial \mathbf{E}} \right] : d\mathbf{E} + \left[\frac{\partial \vec{\mathbf{B}}}{\partial \vec{\mathbf{H}}} - \frac{1}{\frac{\partial \bar{\Xi}}{\partial \alpha}} \frac{\partial \vec{\mathbf{B}}}{\partial \alpha} \otimes \frac{\partial \bar{\Xi}}{\partial \vec{\mathbf{H}}} \right] d\vec{\mathbf{H}} \right|_{n+1}. \quad (40)$$

Evaluating the partial derivatives one observes the algorithmic consistent tangent moduli as

$$\tilde{\mathbb{C}}_{n+1} = \mathbb{C} - \frac{1}{\frac{\partial \bar{\Xi}}{\partial \alpha}} \frac{\partial \mathbf{S}}{\partial \alpha} \otimes \frac{\partial \bar{\Xi}}{\partial \mathbf{E}} \quad (41)$$

$$\tilde{\mathbf{e}}_{n+1} = \alpha_{n+1} \mathbf{e} - \frac{1}{\frac{\partial \bar{\Xi}}{\partial \alpha}} \frac{\partial \mathbf{S}}{\partial \alpha} \otimes \frac{\partial \bar{\Xi}}{\partial \vec{\mathbf{H}}} \quad (42)$$

$$\tilde{\boldsymbol{\mu}}_{n+1} = \boldsymbol{\mu} - \frac{1}{\frac{\partial \bar{\Xi}}{\partial \alpha}} \frac{\partial \vec{\mathbf{B}}}{\partial \alpha} \otimes \frac{\partial \bar{\Xi}}{\partial \vec{\mathbf{H}}}. \quad (43)$$

The derivatives in Eqs. (36) to (43) are given in Appendix D.

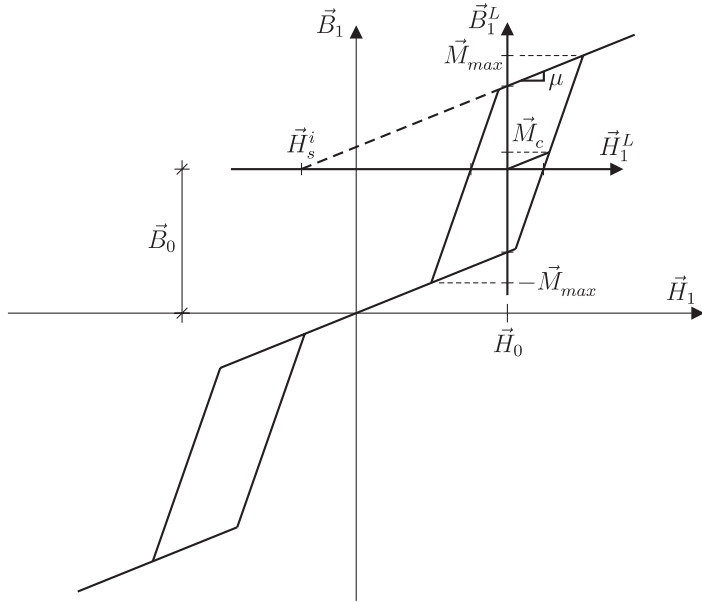


Figure 7: Idealized ferrimagnetic hysteresis with local description

6 Ferrimagnetic hysteresis effects

The presented constitutive model has to be extended to approximate ferrimagnetic hysteresis behavior. The modifications are:

- Introduction of local magnetic field quantities
- Extended switching criterion Φ

The ferrimagnetic hysteresis curve is divided in two separate curves in the first and third quadrant, see Fig. 7. For the approximation a local coordinate system is introduced. Its origin is in the center of the partial hysteresis. The horizontal offset is defined with the parameter \vec{H}_0 . The local field quantities marked with superscript L are defined as

$$\vec{H}^L = \vec{H} - \vec{H}_0 g \mathbf{e} \quad (44)$$

$$\vec{H}^{Li} = \vec{H}^i + \vec{H}_s^i g \mathbf{e}. \quad (45)$$

The scalar valued variable $g = \text{sign}(\vec{H} \cdot \mathbf{e})$ gives the sign of the offset. The offset \vec{B}_0 has not to be specified, because the magnetic flux density is determined by the constitutive equations. The local quantities \vec{H}^L and \vec{H}^{Li} are applied for a local free energy function

$$\begin{aligned} \rho\psi^L = & \frac{1}{2}(\mathbf{E} - \mathbf{E}^i) : \mathbb{C} : (\mathbf{E} - \mathbf{E}^i) + \frac{\vec{H}^i \cdot \mathbf{e}}{H_s^i} (\mathbf{E} - \mathbf{E}^i) : \mathbf{e} \cdot \vec{H}^L \\ & - \frac{1}{2}(\vec{H}^L - \vec{H}^{Li}) \cdot \boldsymbol{\mu} (\vec{H}^L - \vec{H}^{Li}) + \rho\bar{\psi}(\vec{H}^{Li}) \end{aligned} \quad (46)$$

which leads to local dissipation inequality

$$\mathcal{D} = \boldsymbol{\Xi}^L \cdot \vec{\mathbf{H}}^{Li} \geq 0 \quad (47)$$

with

$$\boldsymbol{\Xi}^L = - \left(2 \frac{E_s}{(\vec{H}_s^i)^2} \frac{\partial \rho \psi^L}{\partial \mathbf{E}^i} : \mathbf{I} (\vec{\mathbf{H}}^{Li} - \vec{H}_s^i g \mathbf{e}) + \frac{\partial \rho \psi^L}{\partial \vec{\mathbf{H}}^{Li}} \right). \quad (48)$$

It is noted that $\vec{\mathbf{H}}^i = \vec{\mathbf{H}}^{Li} - \vec{H}_s^i g \mathbf{e}$ is used in the one-to-one relation (9).

The yield criterion is modified to provide reversible behavior in the global origin $\vec{\mathbf{H}} = \mathbf{0}$. Here the sign of g changes. The modified yield criterion reads

$$\Phi^L = \text{sign}(\vec{M}_{max} - \|\vec{\mathbf{M}}^L\|) \frac{\boldsymbol{\Xi}^L \cdot \boldsymbol{\Xi}^L}{(\vec{M}_c)^2} - 1 \leq 0 \quad (49)$$

with $\vec{M}_{max} = \vec{M}_c + k \vec{H}_s^i + a / \text{arctanh}(1/b)$. The vector $\vec{\mathbf{M}}^L = \boldsymbol{\mu}(\vec{\mathbf{H}}^L - \vec{\mathbf{H}}^{Li})$ denotes the uncoupled magnetization. For $\|\vec{\mathbf{M}}^L\| > \vec{M}_c$ the sign function is negative and reversible behavior is ensured. With the Eqs. (46), (49), and the arguments of Section 4 the evolution equation

$$\dot{\vec{\mathbf{H}}}^{Li} = 2 \lambda \text{sign}(\vec{M}_{max} - \|\vec{\mathbf{M}}^L\|) \frac{\boldsymbol{\Xi}^L}{\vec{M}_c} \quad (50)$$

is developed. Analog to Section 4.1 the implicit Euler scheme is applied for the intergration of Eq. (50). The expanded model has no effect on the formulation of the algorithmic consistent tangent moduli of Section 5, because the sign function vanishes with derivation.

7 Constitutive modelling of ferroelectric ceramics

The presented constitutive model is applied almost unmodified for ferroelectric ceramics. Here an additive split is done for the electric field with $\vec{\mathbf{E}} = \vec{\mathbf{E}}^r + \vec{\mathbf{E}}^i$. Furthermore, $\vec{\mathbf{E}}$ and $\vec{\mathbf{E}}^i$ replaces $\vec{\mathbf{H}}$ and $\vec{\mathbf{H}}^i$ in the free energy function Eq. (15). The switching criterion depends on the coercive polarization \vec{P}_c . Due to the phenomenology of ferroelectric ceramics the expanded model of Section 6 is not applied. However, near the Curie temperature ferroelectrics show a similar hysteresis behavior as ferrimagnetics, see Smith (2005).

8 Variational formulation and finite element approximation

In this section the weak form of the coupled boundary value problem is derived. The boundary value problem is given by the balance equations (1) and (2),

the Neumann boundary conditions Eqs. (3) and (4), and Dirichlet boundary conditions

$$\mathbf{u} = \bar{\mathbf{u}} \quad \text{on } \partial_u \mathcal{B}_0 \quad (51)$$

$$\phi = \bar{\phi} \quad \text{on } \partial_\phi \mathcal{B}_0. \quad (52)$$

It holds $\partial \mathcal{B}_0 = \partial_t \mathcal{B}_0 \cup \partial_u \mathcal{B}_0$, $\emptyset = \partial_t \mathcal{B}_0 \cap \partial_u \mathcal{B}_0$, $\partial \mathcal{B}_0 = \partial_\zeta \mathcal{B}_0 \cup \partial_\phi \mathcal{B}_0$ and $\emptyset = \partial_\zeta \mathcal{B}_0 \cap \partial_\phi \mathcal{B}_0$. The weak form $\delta\pi$ is obtained by multiplying Eqs. (1) and (2) with the test functions $\delta\mathbf{u}$ and $\delta\phi$. Integration by part and application of the divergence theorem lead to

$$\begin{aligned} \delta\pi = & \int_{\mathcal{B}_0} \frac{\partial \rho \psi}{\partial \mathbf{E}} : \delta \mathbf{E} + \frac{\partial \rho \psi}{\partial \vec{\mathbf{H}}} \cdot \delta \vec{\mathbf{H}} - \rho \mathbf{b} \cdot \delta \mathbf{u} \, dV \\ & - \int_{\partial_t \mathcal{B}_0} \mathbf{t} \cdot \delta \mathbf{u} \, dA - \int_{\partial_\zeta \mathcal{B}_0} \varsigma_M \cdot \delta \phi \, dA = 0. \end{aligned} \quad (53)$$

The virtual gradient fields are given by $\delta \mathbf{E} = \frac{1}{2}(\nabla \otimes \delta \mathbf{u} + \delta \mathbf{u} \otimes \nabla)$ and $\delta \vec{\mathbf{H}} = -\nabla \delta \phi_M$. The space of the test functions is assumed as

$$\delta \mathcal{U} = \{\delta \mathbf{u} \in [H^1(\mathcal{B}_0)]^3, \delta \mathbf{u}|_{\partial_u \mathcal{B}_0} = \mathbf{0}\} \quad (54)$$

$$\delta \mathcal{V} = \{\delta \phi \in H^1(\mathcal{B}_0), \delta \phi|_{\partial_\phi \mathcal{B}_0} = 0\}. \quad (55)$$

8.1 Element formulation

The finite element approximation is based on the discretization of the domain \mathcal{B}_0 in n_{elem} finite elements \mathcal{B}_e with $\mathcal{B}_0 = \bigcup_{e=1}^{n_{elem}} \mathcal{B}_e$. The shape functions for the presented hexahedral element read

$$N_I = \frac{1}{8} \prod_{i=1}^3 (1 + \xi_I^i \xi^i) \quad \text{with} \quad -1 \leq \xi^i \leq 1 \quad (56)$$

and

$$\begin{aligned} \xi_I^1 &\in \{-1, 1, 1, -1, -1, 1, 1, -1\} \\ \xi_I^2 &\in \{-1, -1, -1, 1, -1, -1, 1, 1\} \\ \xi_I^3 &\in \{-1, -1, -1, -1, 1, 1, 1, 1\}. \end{aligned} \quad (57)$$

Due to the isoparametric concept the same shape function are used for the approximation of the geometry \mathbf{X} and the unknown field quantities $\delta \mathbf{u}$ $\delta \phi$, respectively. This leads to

$$\mathbf{X}_e^h = \sum_{I=1}^8 N_I \mathbf{Y}_I \quad \text{and} \quad \delta \mathbf{d}_e^h = \begin{bmatrix} \delta \mathbf{u}_e^h \\ \delta \phi_e^h \end{bmatrix} = \mathbf{N} \delta \mathbf{v}_e. \quad (58)$$

with $\mathbf{N} = [\mathbf{N}_1, \mathbf{N}_2, \dots, \mathbf{N}_8]$ and $\mathbf{N}_I = \text{diag}[N_I, N_I, N_I, N_I]$. The vector $\delta \mathbf{v}_e = [\delta \mathbf{u}_1^T, \delta \phi_1, \delta \mathbf{u}_2^T, \delta \phi_2, \dots, \delta \mathbf{u}_8^T, \delta \phi_8]^T$ consists of the unknown nodal

degrees of freedom. The nodal coordinates are given by the vector \mathbf{Y}_I . Considering the vector notation of Appendix A the approximated gradient fields read

$$\begin{bmatrix} \delta \mathbf{E}_e^h \\ \delta \vec{\mathbf{H}}_e^h \end{bmatrix} = \mathbf{B} \delta \mathbf{v}_e \quad \text{with} \quad \mathbf{B} = [\mathbf{B}_1, \mathbf{B}_2, \dots, \mathbf{B}_8]. \quad (59)$$

The matrices \mathbf{B}_I consist of derivations of the shape functions to the global coordinates X_i . It holds

$$\mathbf{B}_I = \begin{bmatrix} \mathbf{B}_{Iu} & \mathbf{0} \\ \mathbf{0} & \mathbf{B}_{I\phi} \end{bmatrix} \quad \text{with} \quad \mathbf{B}_{Iu} = \begin{bmatrix} N_{I,X_1} & 0 & 0 \\ 0 & N_{I,X_2} & 0 \\ 0 & 0 & N_{I,X_3} \\ 0 & N_{I,X_3} & N_{I,X_2} \\ N_{I,X_3} & 0 & N_{I,X_1} \\ N_{I,X_2} & N_{I,X_1} & 0 \end{bmatrix} \quad \text{and} \quad \mathbf{B}_{I\phi} = \begin{bmatrix} N_{I,X_1} \\ N_{I,X_2} \\ N_{I,X_3} \end{bmatrix}. \quad (60)$$

The derivations N_{I,X_i} are obtained with $\nabla_X N_I = \mathbf{J}_e^{-1} \nabla_\xi N_I$. The matrix \mathbf{J}_e is the Jacobian given by

$$\mathbf{J}_e = \nabla_\xi \otimes \mathbf{X}_e^h \quad \text{with} \quad \nabla_\xi = \left[\frac{\partial}{\partial \xi^1}, \frac{\partial}{\partial \xi^2}, \frac{\partial}{\partial \xi^3} \right]^T. \quad (61)$$

Considering the before mentioned interpolation the weak form on element level is approximated by

$$\delta \pi_e^h = \delta \mathbf{v}_e^T \underbrace{\left[\int_{\mathcal{B}_e} \mathbf{B}^T \begin{bmatrix} \frac{\partial \rho \psi}{\partial \mathbf{E}} \\ \frac{\partial \rho \psi}{\partial \vec{\mathbf{H}}} \end{bmatrix} - \mathbf{N}^T \begin{bmatrix} \rho \mathbf{b} \\ 0 \end{bmatrix} \right] dV - \int_{\partial \mathcal{B}_e} \mathbf{N}^T \begin{bmatrix} \mathbf{t} \\ \varsigma_M \end{bmatrix} dA}_{\mathbf{R}_e^h}. \quad (62)$$

After assembly over all elements one obtain the global weak form $\delta \pi^h = \bigcup_{e=1}^{nelm} \delta \pi_e^h$ with the global residual vector $\mathbf{R}^h = \bigcup_{e=1}^{nelm} \mathbf{R}_e^h$ and the global nodal degrees of freedom $\delta \mathbf{v} = \bigcup_{e=1}^{nelm} \delta \mathbf{v}_e$. Due to the nonlinear constitutive model the equation $\delta \pi^h = 0$ is solved iteratively. The unknown node values \mathbf{v}_{n+1} for the load step t_{n+1} are estimated by a Newton-Raphson scheme. The residual vector \mathbf{R}^h is expanded by a Taylor series which is truncated after the linear term

$$\mathbf{R}_{n+1}^{h(K)} + \frac{\partial \mathbf{R}^{h(K)}}{\partial \mathbf{v}_{n+1}} \Delta \mathbf{v}_{n+1}^{(K)} = \mathbf{0}. \quad (63)$$

After each iteration step (K) the nodal degrees of freedom are updated by $\mathbf{v}_{n+1}^{(K+1)} = \mathbf{v}_{n+1}^{(K)} + \Delta \mathbf{v}_{n+1}^{(K)}$. The start value is obtained from the last state of equilibrium $\mathbf{v}_{n+1}^{(1)} = \mathbf{v}_n$. The approximations of the incremental gradient fields $[\Delta \mathbf{E}_e^T, \Delta \vec{\mathbf{H}}_e^T]^T = \mathbf{B} \Delta \mathbf{v}_e$ are analog to Eq. (59). The tangent stiff matrix on element level reads

$$[\mathbf{K}_{eT}]_{n+1}^{(K)} := \frac{\partial \mathbf{R}^{h(K)}}{\partial \mathbf{v}_{n+1}} = \left[\int_{\mathcal{B}_e} \mathbf{B}^T \tilde{\mathbb{D}} \mathbf{B} dV \right]_{n+1}^{(K)} \quad \text{with} \quad \tilde{\mathbb{D}}_{n+1}^{(K)} = \begin{bmatrix} \tilde{\mathbb{C}} & \tilde{\mathbf{e}} \\ \tilde{\mathbf{e}}^T & \tilde{\boldsymbol{\mu}} \end{bmatrix}_{n+1}^{(K)} \quad (64)$$

The algorithmic consistent tangent moduli $\tilde{\mathbb{C}}$, $\tilde{\mathbf{e}}$ and $\tilde{\boldsymbol{\mu}}$ for t_{n+1} are evaluated with Eqs. (41)-(43).

The element formulation for ferroelectric ceramics is based on an equivalent variational approach as applied for magnetostrictive alloys. Instead of \vec{H} the electric field strength \vec{E} is used which is described with the electric scalar potential ϕ_E , see Eq. (13). The local Gauss' law (11) and the boundary condition (12) replaces the solenoidality of the magnetic field and the corresponding boundary condition, see Eqs. (2) and (4). This leads to a finite element approximation which differs only in the used field quantities from the one of Section 8.1.

9 Numerical simulations

The developed finite element formulation is implemented in the finite element code FEAP which is documented in [Taylor \(2008\)](#). In the following, different examples are used to show the capabilities of the proposed constitutive model. The first example deals with the nonlinear behavior of the magnetostrictive alloy Terfenol-D. The occurring hysteresis curves are compared with experimental data. An approximation of ferrimagnetic behavior is discussed in further simulations. In the second example a specimen consisting out of a ferroelectric ceramic is analyzed. The results show that the model is able to reproduce the typical hysteresis curves of ferroelectric ceramics correctly. In the third example an amplified magnetostrictive actuator is presented. To improve the design it is optimized in a parametric study. In the fourth example a piezoelectric hollow cylinder of soft lead lanthanum zirconate titanate is considered. The borders of these cylinders tend to warp inwardly during polarization. This effect will be discussed by means of the results. The fifth example deals with a piezoelectric telescope actuator. The results of the nonlinear simulation are compared with experimental data.

9.1 Magnetostrictive hysteresis

A simple example is used to illustrate the ability of the presented constitutive model to account for magnetostrictive hysteresis phenomena. Here a cube of Terfenol-D with an edge length of $L = 20$ mm is considered. The boundary and loading conditions are given in Fig. 8. The magnetic loading is set with the scalar potential $\bar{\phi}_M$ resulting in a homogeneous magnetic field in 3-direction. The field strength is oscillated in a zigzag function between $\vec{H}_3 = -100$ kA/m and $\vec{H}_3 = 100$ kA/m. The applied material parameters based on [Dapino et al. \(2006\)](#) and [Moffett et al. \(1991\)](#) are given in Tab. 1. The resulting hysteresis curves compared with the experimental data of [Engdahl \(2000\)](#) are depicted in Fig. 9. Terfenol-D is a soft magnetic material. Thus, the range of linear behavior is very small. Raising the magnetic field beyond the coercive value \vec{M}_c results in an intense increase of \vec{B}_3 and \vec{E}_{33} . The growth slows down for

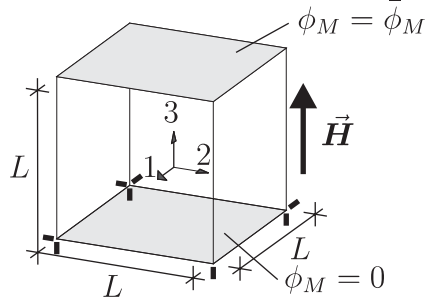


Figure 8: Boundary and loading conditions for the Terfenol-D specimen

Terfenol-D

$E_1 = E_3 = 29 \text{ GN/m}^2$, $\nu_{12} = \nu_{13} = 0.25$, $G_{12} = G_{13} = 11.6 \text{ GN/m}^2$
$\epsilon_{33} = 40.9 \text{ Vs/Am}^2$, $\epsilon_{13} = -43.95 \text{ Vs/Am}^2$, $\epsilon_{51} = 28.3 \text{ Vs/Am}^2$
$\mu_1 = \mu_2 = \mu_3 = 2.8025 \cdot 10^{-6} \text{ Vs/Am}$
$\vec{M}_c = 8.2 \cdot 10^{-3} \text{ T}$, $E_s^i = 1.08 \cdot 10^{-3}$, $\vec{H}_s^i = 185 \text{ kA/m}$ $k = 1.03 \mu_3$
$a = 0.15/\text{arctanh}(1/b) \text{ T}$, $b = 1.04$

Table 1: Applied material parameters

values $\vec{H}_3 > 50 \text{ kA/m}$, because of the arctanh-term in the hardening function. This leads to a saturation of the irreversible quantity α for magnetic fields higher 80 kA/m . After unloading only low remanent values of \vec{B}_3 and E_{33} are noticed. The ferromagnetic and butterfly hysteresis in Fig. 9 show good agreement with the experimental data. It confirms that the model is able to approximate the typical behavior of Terfenol-D.

A further aspect of this examples is the convergence behavior of the presented constitutive model. For this, a load step from $\vec{H}_3 = 5 \text{ kA/m}$ to $\vec{H}_3 = 11 \text{ kA/m}$ is considered, which is within a range of high nonlinear growing. The interval is marked by dots in Fig. 9. The residua of the iteration processes are used to evaluate the convergence rates. The norms of the residuum vector \mathbf{R} of the global iteration are listed in the first column of Tab. 2. A typical local iteration is summarized on the right hand side. Therefore the residua of Eq. (30) are considered. It is noted that quadratic convergence is obtained for all residua.

Terfenol-D shows ferrimagnetic behavior for mechanical prestresses . The presented simulations account for different values of the parameter \vec{H}_0 . The remaining parameters are modified according to Tab. 3. The results are given in Fig. 10. Depending on the offset \vec{H}_0 the separated hysteresis curves are shifted differently, which represents qualitatively the occurring material behavior. As mentioned before the model does not include the influence of the mechanical prestress. For this reason the curves are not compared with experimental data.

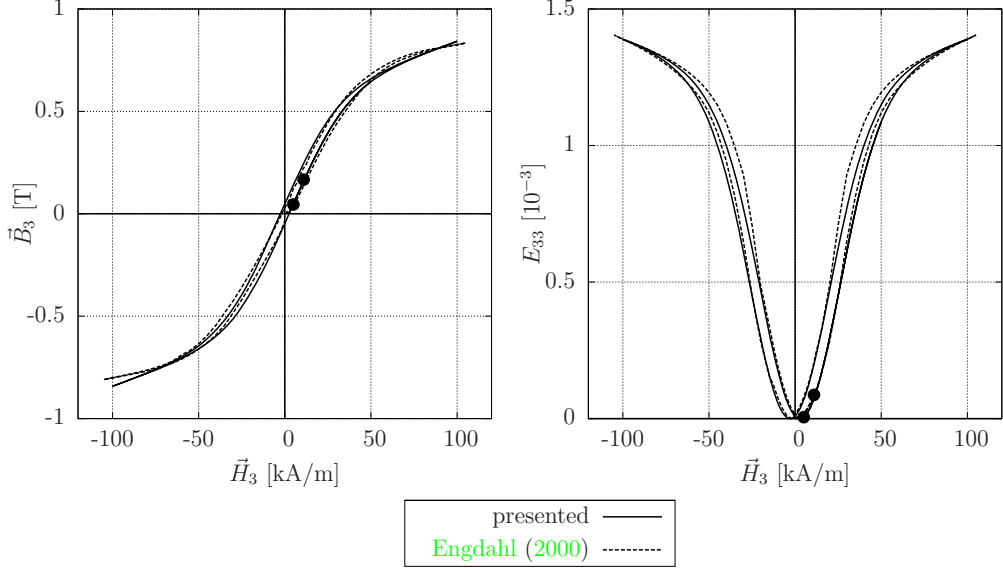


Figure 9: Ferromagnetic and butterfly hysteresis compared to experimental data and the load step for convergence evaluation

iteration	global iteration $\ \mathbf{R}\ $	local iteration	
		R_a	R_b
1	$9.904572E + 01$	$-7.196267E - 02$	$1.052652E + 00$
2	$1.732041E + 02$	$-3.088828E - 02$	$9.670525E - 02$
3	$7.862738E + 00$	$-1.770798E - 03$	$1.616275E - 03$
4	$2.152431E - 02$	$-1.583016E - 06$	$4.965618E - 07$
5	$1.636638E - 07$	$-4.076455E - 13$	$4.820135E - 14$

Table 2: Convergence of the local and the global iteration process

9.2 Ferroelectric hysteresis

This examples is concerned with the simulation of ferroelectric ceramics. A cubic specimen of lead lanthanum zirconate titanate (PLZT) is simulated. The edge length is $L = 10$ mm. The boundary conditions are analogue to Fig. 8 but ϕ_E is used instead of ϕ_M . The scalar potential $\bar{\phi}_E$ at the topside is oscillating between ± 800 V. The material parameters are given in Tab. 4. Fig. 11 shows the resulting ferroelectric und butterfly hysteresis compared with the results of [Hwang et al. \(1995\)](#). A good agreement for both curves is observed. PLZT has a much higher coercive value than Terfenol-D which results in distinctive

$$\begin{aligned} E_s^i &= 0.35 \cdot 10^{-3}, \quad \vec{H}_s^i = 125 \text{ kA/m} \quad k = 1.1 \mu_3 \\ a &= 0.1/\text{arctanh}(1/b) \text{ T}, \quad b = 1.05 \end{aligned}$$

Table 3: Modified material parameters of the hardening function for ferrimagnetic behavior

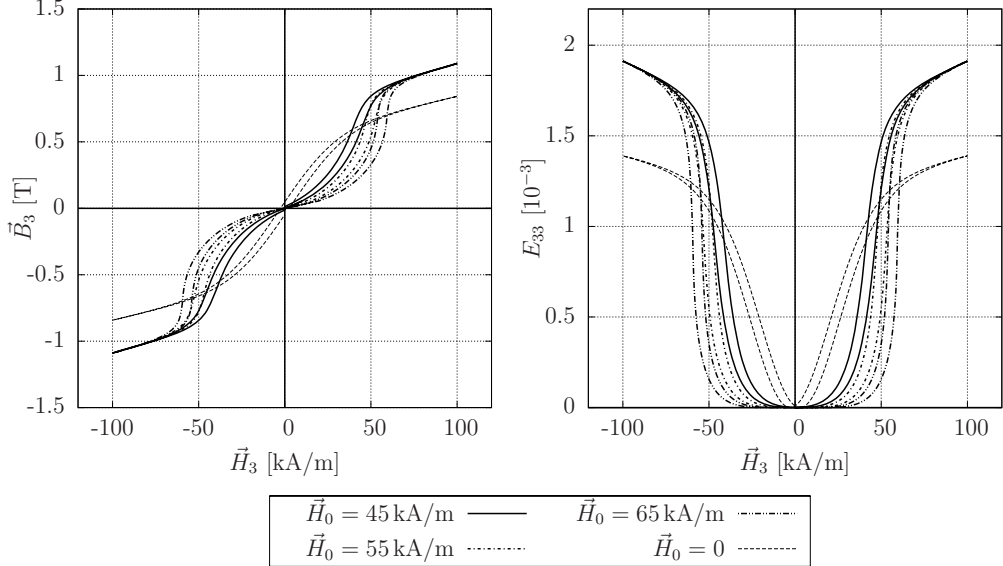


Figure 10: Ferrimagnetic and butterfly hysteresis for different parameters \vec{H}_0

PLZT

$E_1 = E_3 = 68 \text{ GN/m}^2$	$\nu_{12} = \nu_{13} = 0.35$	$G_{13} = 25.19 \text{ GN/m}^2$
$\epsilon_{33} = 50.116 \text{ C/m}^2$	$\epsilon_{13} = -14.96 \text{ C/m}^2$	$\epsilon_{51} = 38.148 \text{ C/m}^2$
$\epsilon_1 = \epsilon_2 = \epsilon_3 = 1.125 \text{ C/kN m}^2$		
$\vec{P}_c = 0.405 \cdot 10^{-3} \text{ C/m}^2$	$E_s^i = 1.44 \cdot 10^{-3}$	$\vec{E}_s^i = 0.215 \text{ kV/m}$
$a = 0.0005/\text{arctanh}(1/b) \text{ C/m}^2$		$k = 0.9998 \epsilon_3$
		$b = 1.04$

Table 4: Applied material parameters for PLZT

remanent values of \vec{D}_3 and E_{33} .

9.3 Amplified magnetostrictive actuator

The displacements which can be achieved with magnetostrictive and piezoelectric materials are only small. Different approaches are used to increase the working range of actuator devices. One possibility is a mechanical amplified actuator. An optimized design for such an device is discussed in the following example. The amplification is accomplished by a special frame, which increases the achieved displacements of the device, see Fig. 12.

The dotted outline represents the undeformed initial state. With application of a magnetic field the magnetostrictive element in the center changes its length. The magnetic field is induced homogeneously by a surrounding coil, which is not shown in the plot. The contraction of the magnetostrictive rod causes a movement w of the adapter plates. This movement is higher than the deformation of the active material. In the following an own design is discussed which is based on an actuator of Energen, Inc. The used active material is Terfenol-D. The influence of the height of the frame on the mechanical proper-

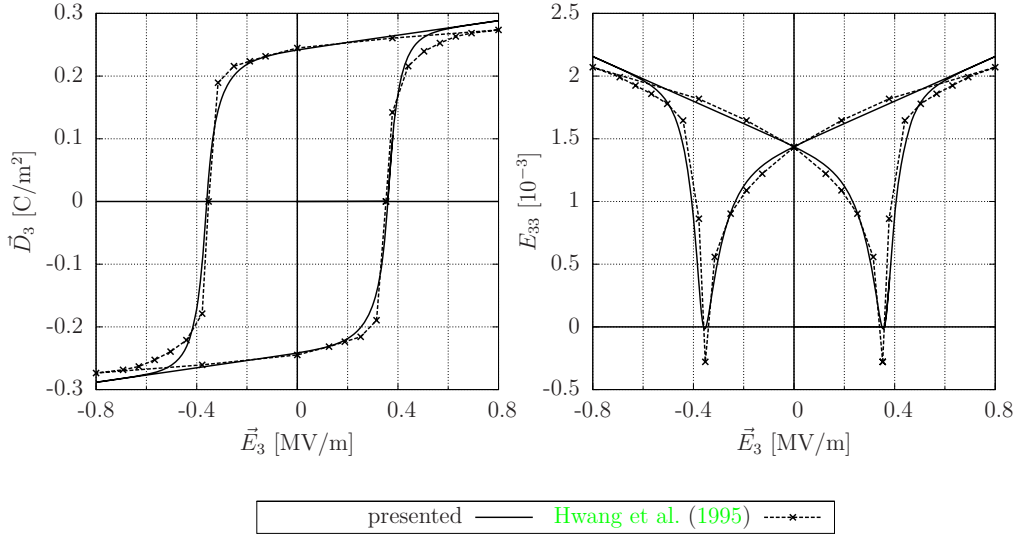


Figure 11: Ferroelectric und butterfly hysteresis compared to experimental data

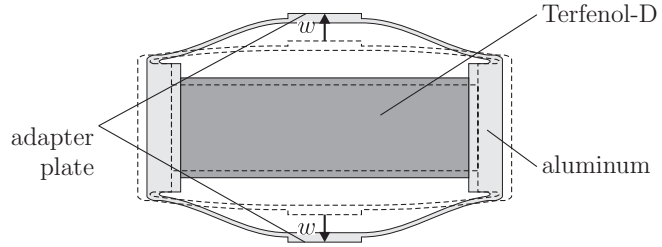
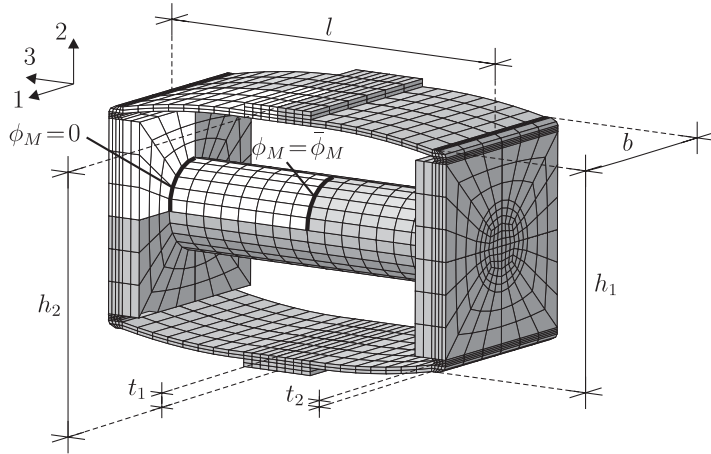


Figure 12: Functioning of an amplified actuator

ties of actuator is examined in a parametric study. The aim is to determine the optimal design for maximal amplitudes of displacement and force. The chosen geometry and finite element mesh are given in Fig. 13. The Terfenol-D rod has a length of 50 mm and a diameter of 14 mm. With respect to symmetry only an eighth of the actuator is modeled with 654 hexahedral elements. This area is depicted white in Fig. 13. The simulations have shown that a further mesh refinement has no significant impact on the results. The displacements perpendicular to the symmetry plane are fixed at the symmetry borders. By setting the scalar potential $\phi_M = \bar{\phi}_M$ at one end of the Terfenol-D rod a homogeneous magnetic field in the rod is applied. The maximal field strength is 100 kA/m. The material parameters for Terfenol-D are given in Tab. 1. The characteristics of aluminum are modeled with $E = 75000 \text{ N/mm}^2$ and $\nu = 0.33$. The deformed structure for $\vec{H}_3 = 100 \text{ kA/m}$ is depicted in Fig. 14. The influence of the height h_2 on the maximal displacements w is tested in the first part of the parametric study. The driven load cycle for \vec{H}_3 is 0, 100 kA/m, 0. The height h_2 is varied between 38 mm and 44 mm. The resulting load displacement curves are depicted in Fig. 15. The nonlinear material model causes hysteresis



Dimensions: $l = 61 \text{ mm}$, $b = 30 \text{ mm}$, $h_1 = 34 \text{ mm}$
 $t_1 = 1 \text{ mm}$, $t_2 = 2.2 \text{ mm}$

Figure 13: Geometry and finite element mesh of the presented actuator

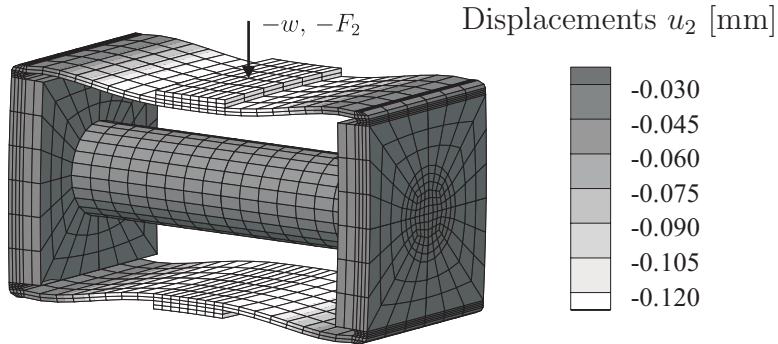


Figure 14: Deformed structure for $\vec{H}_3 = 100 \text{ kA/m}$ und $h_2 = 41 \text{ mm}$, the displacements are scaled by factor 30

effects for w , which affect in particular the range between 10 to 70 kA/m. The amplitude of the hysteresis depends on h_2 . The maximal values of w can be achieved by devices with a height $h_2 = 41 \text{ mm}$. Higher values of h_2 decrease the maximal displacements.

The second aspect of this example is the influence of the height h_2 on the forces F_2 which can be achieved with the actuator. In this case a working point of $\vec{H}_3 = 50 \text{ kA/m}$ is considered. First of all the Terfenol-D rod is magnetized with a field strength of 100 kA/m. Then the load is reduced to the working point. Now the adapter is fixed in w -direction at the current deformed position and a further load cycle between 25 and 75 kA/m is driven. The reaction forces F_2 at the adapter plates are plotted in Fig. 16. Again hysteresis effects are observed arising from the nonlinear constitutive model. An increasing height h_2 causes higher forces F_2 . But a heightening above $h_2 = 46 \text{ mm}$ has only low

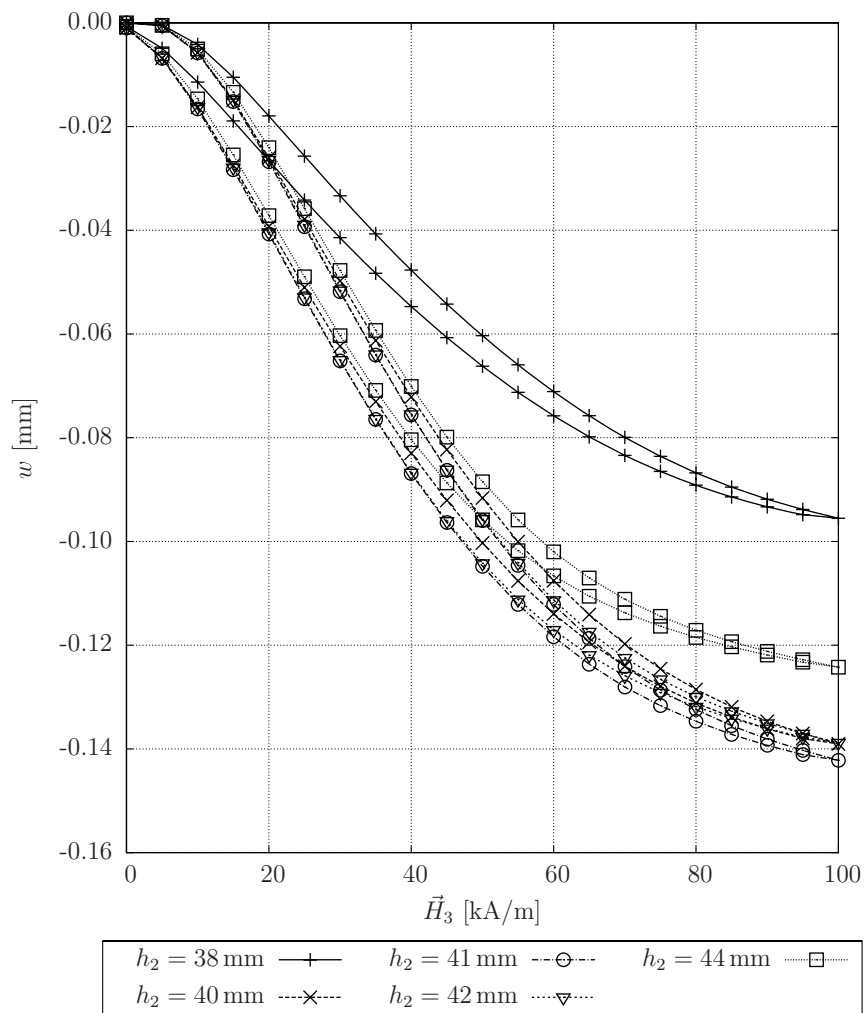


Figure 15: Displacements w for different values h_2

effect on F_2 .

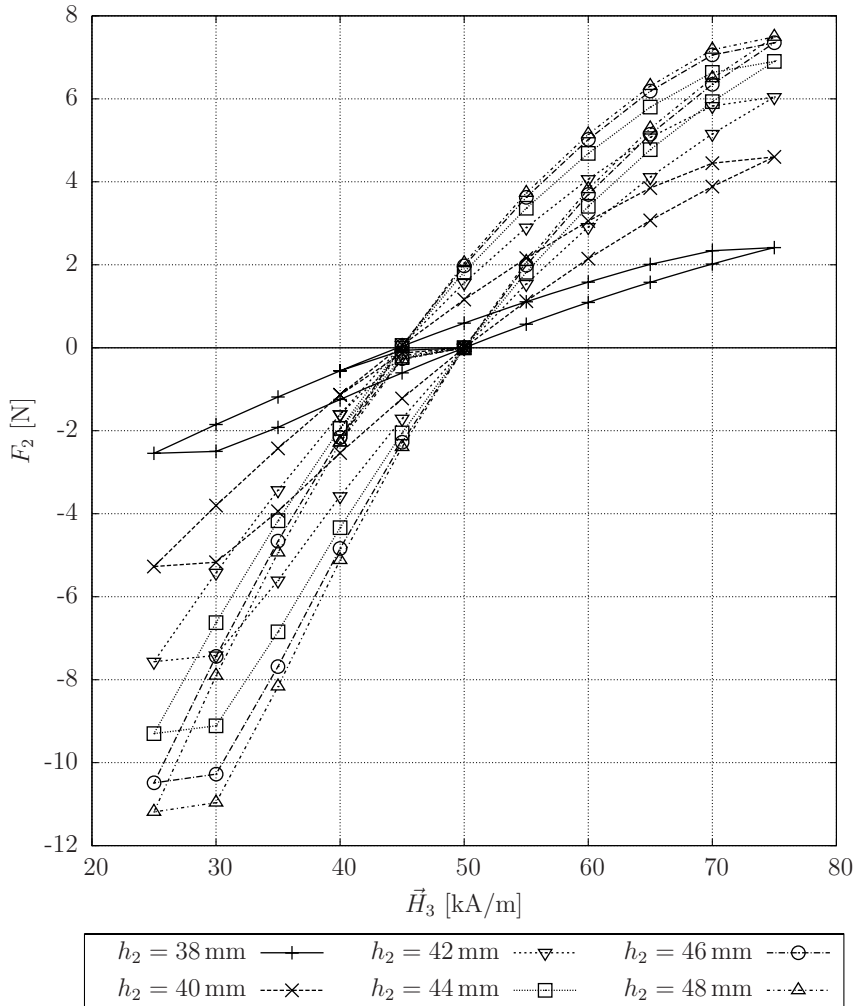


Figure 16: Forces at the adapter for different values h_2

9.4 Piezoelectric hollow cylinder

A piezoelectric hollow cylinder of soft lead zirconate titanate (PZT) is considered. The borders of these cylinders tend to warp inwardly during polarization. This behavior will be discussed and the results will be compared with simulations of Laskewitz et al. (2006). The geometry, boundary and loading conditions are depicted in Fig. 17. With respect to rotational symmetry only one element is used in circumferential direction. The material parameters are chosen analog to Laskewitz et al. (2006), see Tab. 5. The local 3-direction of the material and the polarization direction e are parallel to radial direction r . Fig. 18 shows the deformed structure scaled by factor 30. In Fig. 18a) the cylinder is maximal loaded with $\bar{\phi}_E = 4.5 \text{ kV}$. Fig. 18b) depicts the structure after unloading. In both cases a warping of the upper boundary inwardly is noticed. This behavior can be explained with the logarithmic distribution of the electric potential in radial direction which results from the analytical solu-

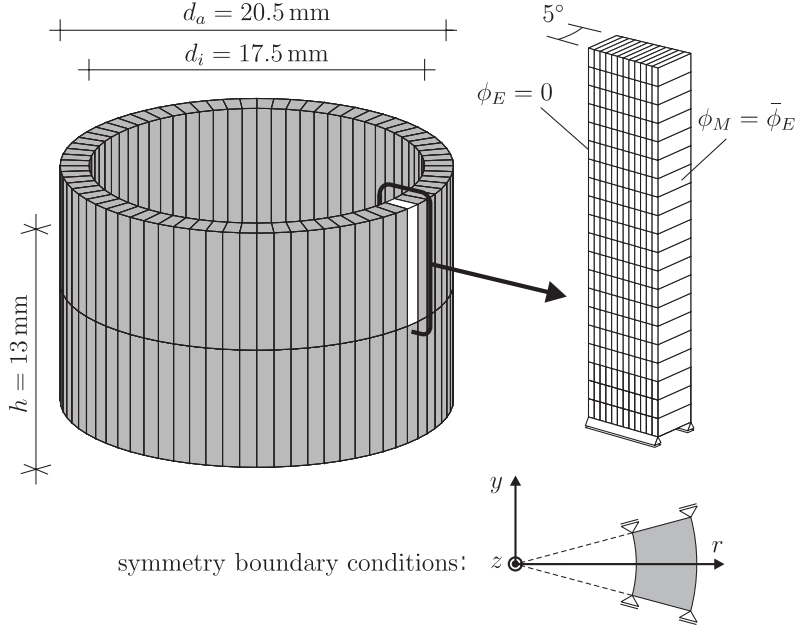


Figure 17: Geometry and finite element mesh of the presented actuator

$E_1 = E_3 = 0.06 \text{ MN/mm}^2$, $\nu_{12} = \nu_{13} = 0.396$, $G_{13} = 0.02149 \text{ MN/mm}^2$
$e_{33} = 21.796 \cdot 10^{-6} \text{ C/mm}^2$, $e_{13} = -6.571 \cdot 10^{-6} \text{ C/mm}^2$
$e_{51} = 12.464 \cdot 10^{-6} \text{ C/mm}^2$
$\epsilon_1 = \epsilon_2 = 1.27796 \cdot 10^{-9} \text{ C/MN mm}^2$, $\epsilon_3 = 0.74409 \cdot 10^{-9} \text{ C/MN mm}^2$
$\vec{P}_c = 7.4409 \cdot 10^{-9} \text{ C/mm}^2$, $E_s^i = 1.2 \cdot 10^{-3}$, $\vec{E}_s^i = 38.9736 \text{ MN/C}$, $k = 1.00001 \epsilon_3$
$a = 0.2 \cdot 10^{-8} \text{ C/mm}^2$, $b = 1.0$

Table 5: Applied material parameters for the hollow cylinder

tion of the governing Laplace equation $\nabla^2 \phi_E = 0$. The electric field \vec{E}_3 at the inner boundary is higher than \vec{E}_3 at the outer boundary. This causes a higher piezoelectric contraction inboards.

In Fig. 19 the normalized polarization $|\alpha|$ is plotted versus r . The results of Laskewitz et al. (2006) are given for comparison. At full loading the material is completely polarized across the entire width, see Fig. 19a). With unloading the outer area begins to depolarize as depicted in Fig. 19b). Here the presented results show a smoother transition compared to Laskewitz et al. (2006) which is caused by the arctanh function in the hardening function. In Fig. 20 the ferroelectric hysteresis are plotted at the discrete positions (I) and (II) marked in Fig. 19. The dotted part of the curve is the passed range. In (I) the electric field rises much higher than in (II). Furthermore in (I) a positive electric field remains after unloading whereas a negative one is noticed in (II). This negative electric field causes the slight depolarization at the outer boundary. A similar behavior is noticed for the relating butterfly hysteresis, see Fig. 21. Here the strain component E_{33} and accordingly the transversal contraction are much

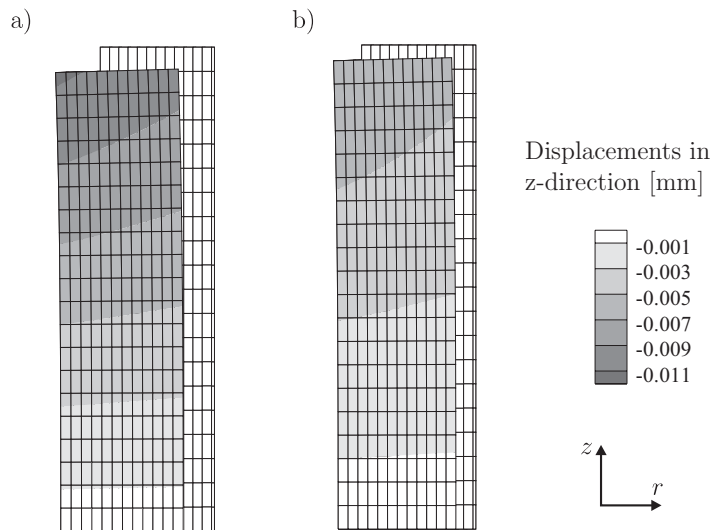


Figure 18: Deformed cylinder scaled by factor 30 compared with undeformed structure: a) at maximal loading $\bar{\phi}_E = 4.5 \text{ kV}$, b) after unloading $\bar{\phi}_E = 0$

higher in (I) than in (II). So we have a remaining warping of the cylinder after unloading.

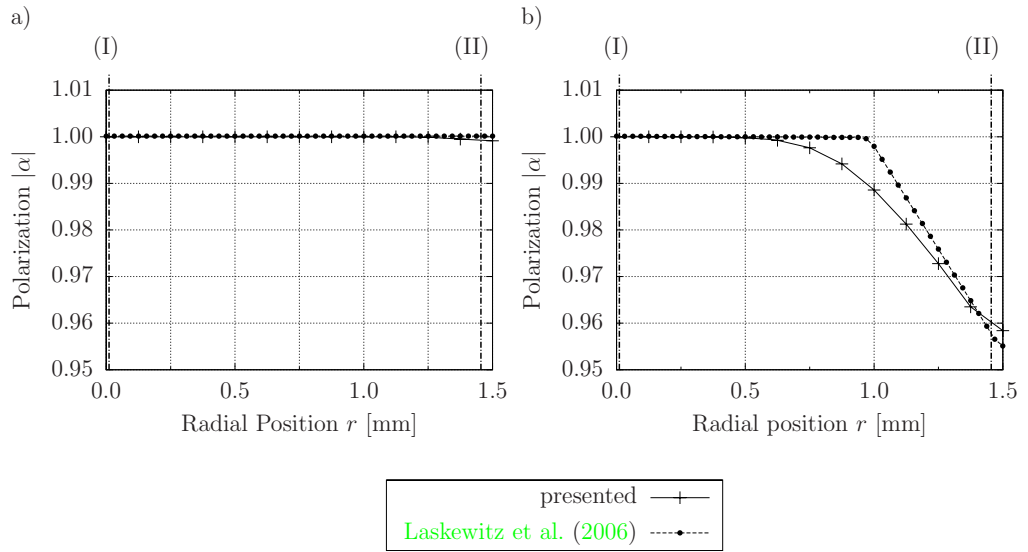


Figure 19: Normalized polarization r -direction: a) maximal loading $\bar{\phi}_E = 4.5 \text{ kV}$, b) after unloading $\bar{\phi} = 0$

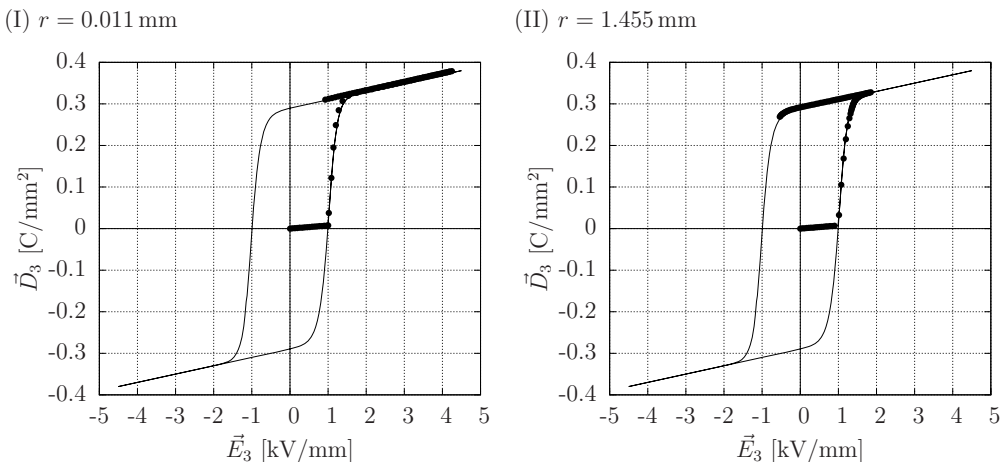


Figure 20: Ferroelectric hysteresis at (I) and (II)

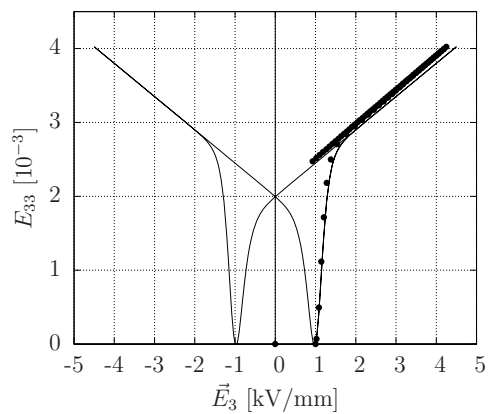
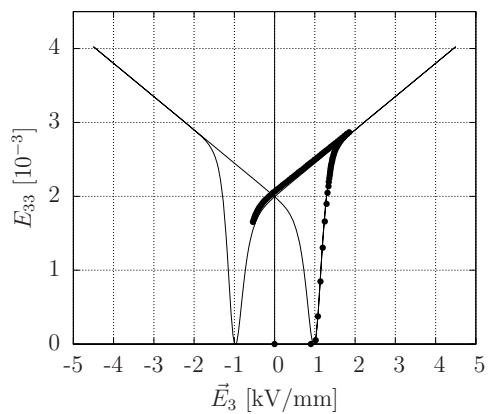
(I) $r = 0.011 \text{ mm}$ (II) $r = 1.455 \text{ mm}$ 

Figure 21: Butterfly hysteresis at (I) and (II)

9.5 Piezoelectric telescope actuator

Telescope actuators are a common design for actuators. They consist of concentric cylinders connected by end-caps. The idea of the design is an alternating contraction respectively extension of the cylinders by an electric loading to amplify the achievable displacements. In this example a telescope actuator fabricated by injection molding is discussed. The design is presented by Alexander et al. (2001). The geometry with dimensions and outer diameters are depicted in Fig. 22. With respect to symmetry only a quarter of 90° is meshed with 430 hexahedral elements. The examined displacement is w .

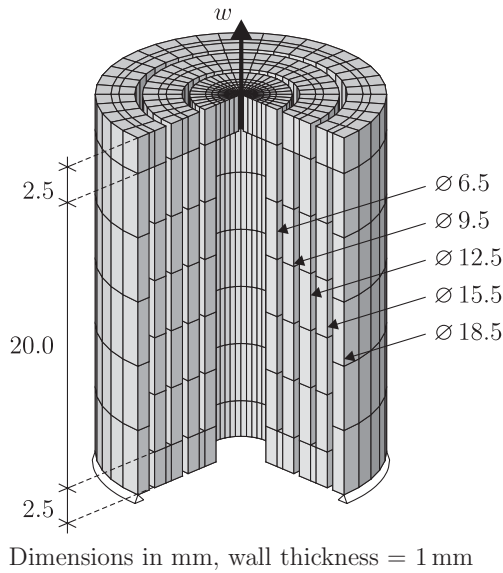


Figure 22: Geometry and finite element mesh of the telescope actuator

The applied material parameters for the ferroelectric ceramic MSI-53HD are given in Tab. 6 and are estimated on the basis of Alexander et al. (2001). The privileged 3-direction of the material points is the radial direction. Unlike the conventional manufactured actuators the injection molded design is polarized after fabrication. To polarize the cylinders a radial electric field of $E_3 = 1200 \text{ V/mm}$ is applied. Later on an electric field of $E_3 = 300 \text{ V/mm}$ is used for the working mode. The electric potential is applied by nickel electrodes as depicted in Fig. 23a). The resulting deformation scaled by factor 100 is given in Fig. 23b). The displacement w is plotted across the electric field for the loading cycle $\vec{E}_3 = 0, 300 \text{ V/mm}, -300 \text{ V/mm}, 0$. The results are depicted in Fig. 24. Due to the nonlinear constitutive law hysteresis effects are observed in the plot, which show good agreement with the experimental results of Alexander et al. (2001). The linear analytical solution of Alexander et al. (2001) can not reproduce hysteresis effects. It is noted that the presented results are moved by $9.545 \mu\text{m}$ to account for the deformation following from the polarization process. The nonlinear behavior results from a depolariza-

$E_1 = 60606 \text{ N/mm}^2$, $E_3 = 48310 \text{ N/mm}^2$, $\nu_{12} = 0.290$, $\nu_{13} = 0.408$
$G_{13} = 22990 \text{ N/mm}^2$
$\varepsilon_{33} = 10.63 \cdot 10^{-6} \text{ C/mm}^2$, $\varepsilon_{13} = -29.88 \cdot 10^{-6} \text{ C/mm}^2$, $\varepsilon_{51} = 27.26 \cdot 10^{-6} \text{ C/mm}^2$
$\epsilon_1 = \epsilon_2 = \epsilon_3 = 1.0693 \cdot 10^{-14} \text{ C/N mm}^2$
$\vec{P}_c = 0.7693 \cdot 10^{-8} \text{ C/mm}^2$
$E_s^i = 1.2 \cdot 10^{-3}$, $\vec{E}_s^i = 17.63507 \text{ V/mm}$, $k = 1.006 \epsilon_3$
$a = 0.0099 \cdot 10^{-6}/\text{arctanh}(1/b) \text{ C/mm}^2$, $b = 1.0005$

Table 6: Applied material parameters for MSI-53HD

tion during the loading cycle. In Fig. 25a) the normalized polarization in the cylinders is plotted for $\vec{E}_3 = 300 \text{ V/mm}$. In the cylinder 2 and 4 the electrical field points opposite to the direction of polarization. As a result the polarization decrease to 95%. For a loading in the opposite direction with $\vec{E}_3 = -300 \text{ V/mm}$ the remaining cylinders are depolarized, see Fig. 25b). This depolarization of the cylinders is completed after one load cycle. A recurring minor hysteresis obtained in Alexander et al. (2001) can not be approximated, since this behavior is not considered within the constitutive model.

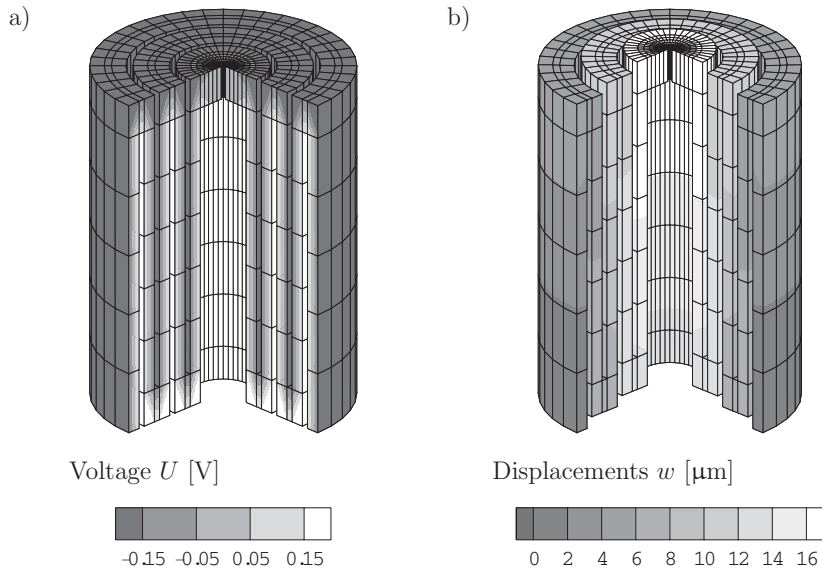


Figure 23: Energized actuator, $\vec{E} = 300 \text{ V/mm}$: a) loading condition b) deformed actuator, displacements scaled by factor 100

10 Conclusion

In this paper a nonlinear constitutive model for magnetostrictive and piezoelectric materials is presented. Beside the general approach an additive split

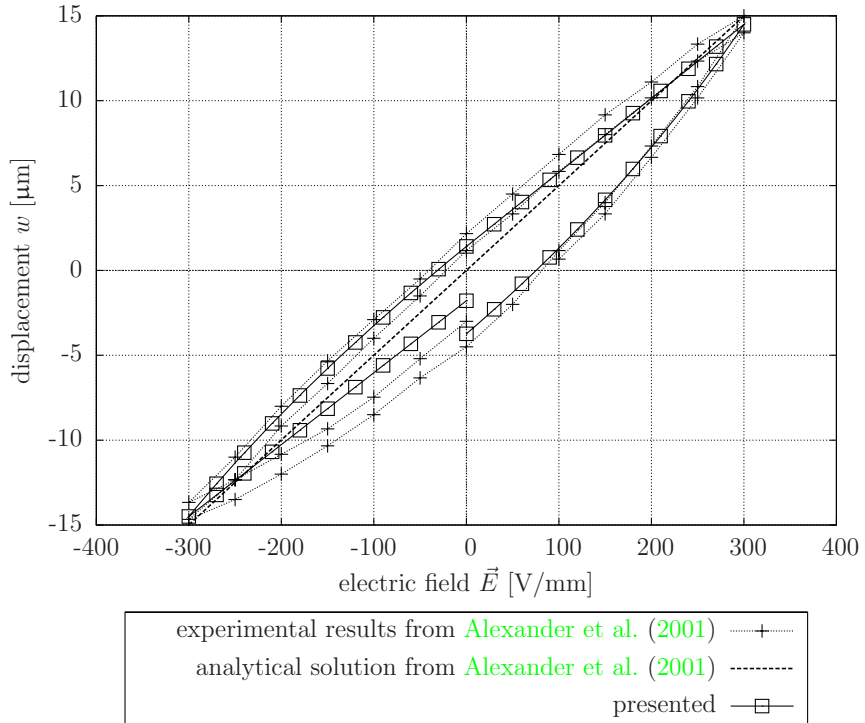


Figure 24: Hysteresis behavior of the telescope actuator in comparison with [Alexander et al. \(2001\)](#)

of the field strength in a reversible and an irreversible part is a novel aspect of the proposed macroscopic model. The irreversible part serves as internal variable describing the domain state of the material. The additive split of the field strength allows a consistent finite element approximation employing displacements and scalar potential as independent variables. The irreversible strains which arises from domain switching processes are determined by the irreversible field strength with a one-to-one relation. The model is embedded in a thermodynamic consistent framework, which is based on the definition of a free energy function and a switching criterion. It is able to reproduce the ferroelectric and butterfly hysteresis of ferroelectric ceramics. For the simulation of magnetostrictive materials an expansion is proposed which includes ferrimagnetic behavior. The model is incorporated in a finite element formulation. The algorithmic consistent tangent moduli are given in closed form. In the presented numerical examples the results are compared with experimental data, which demonstrate the capability of the formulation.

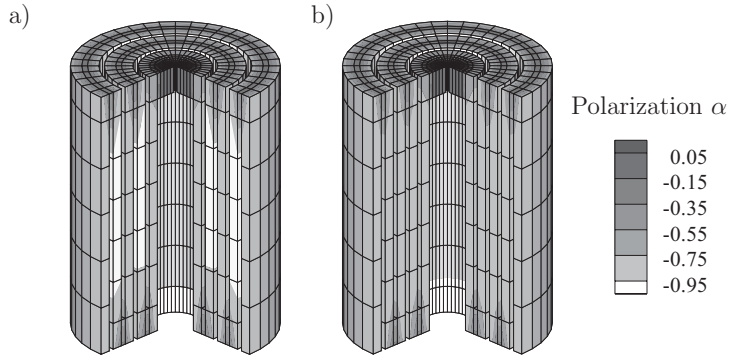


Figure 25: Polarisation in the actuator: a) $\vec{E} = 300 \text{ V/mm}$ b) $\vec{E} = -300 \text{ V/mm}$

A Vector notation and linear material constants

Vector notation of the strain and stress tensor:

$$\mathbf{E} = [E_{11}, E_{22}, E_{33}, 2E_{23}, 2E_{13}, 2E_{12}]^T \quad (65)$$

$$\mathbf{S} = [S_{11}, S_{22}, S_{33}, S_{23}, S_{13}, S_{12}]^T \quad (66)$$

Elasticity tensor in matrix form:

$$\mathbb{C}^{-1} = \begin{bmatrix} \frac{1}{E_1} & -\frac{\nu_{12}}{E_1} & -\frac{\nu_{13}}{E_3} & 0 & 0 & 0 \\ -\frac{\nu_{12}}{E_1} & \frac{1}{E_1} & -\frac{\nu_{13}}{E_3} & 0 & 0 & 0 \\ -\frac{\nu_{13}}{E_3} & -\frac{\nu_{13}}{E_3} & \frac{1}{E_3} & 0 & 0 & 0 \\ 0 & 0 & 0 & \frac{1}{G_{13}} & 0 & 0 \\ 0 & 0 & 0 & 0 & \frac{1}{G_{13}} & 0 \\ 0 & 0 & 0 & 0 & 0 & \frac{1}{G_{12}} \end{bmatrix} \quad (67)$$

with $G_{12} = \frac{E_1}{2(1+\nu_{12})}$.

Piezomagnetic respectively piezoelectric couple tensor in matrix form, magnetic permeability and electric permittivity:

$$\mathbf{e} = \begin{bmatrix} 0 & 0 & e_{13} \\ 0 & 0 & e_{13} \\ 0 & 0 & e_{33} \\ 0 & e_{51} & 0 \\ e_{51} & 0 & 0 \\ 0 & 0 & 0 \end{bmatrix}, \quad \boldsymbol{\mu} = \begin{bmatrix} \mu_1 & 0 & 0 \\ 0 & \mu_2 & 0 \\ 0 & 0 & \mu_3 \end{bmatrix}, \quad \boldsymbol{\epsilon} = \begin{bmatrix} \epsilon_1 & 0 & 0 \\ 0 & \epsilon_2 & 0 \\ 0 & 0 & \epsilon_3 \end{bmatrix} \quad (68)$$

B Scalar valued conjugated variable to the internal variable

$$\begin{aligned}\bar{\Xi} = & -\mathbf{I} : \left[\mathbb{C} : \mathbf{I} 2\alpha^3 E_s - \mathbf{e} \cdot \vec{\mathbf{H}} 3\alpha^2 - \mathbb{C} : \mathbf{E} 2\alpha \right] \frac{E_s}{\vec{H}_s^i} \\ & - \vec{\mathbf{H}} \cdot \mathbf{e}^T : \left[\mathbf{E} - \mathbf{I} E_s \alpha^2 \right] \frac{1}{\vec{H}_s^i} - \mathbf{e} \cdot \boldsymbol{\mu} (\vec{\mathbf{H}} - \mathbf{e} \vec{H}_s^i \alpha) \\ & - \frac{\partial \rho \psi}{\partial \vec{\mathbf{H}}^i} \cdot \mathbf{e} \vec{H}_s^i\end{aligned}\tag{69}$$

$$\begin{aligned}\frac{\partial \bar{\Xi}}{\partial \alpha} = & -2 \frac{E_s}{\vec{H}_s^i} \mathbf{I} : \left[\mathbb{C} : \mathbf{I} 3\alpha^2 \mathbf{E}_s - \mathbf{e} \cdot \vec{\mathbf{H}} 3\alpha - \mathbb{C} : \mathbf{E} \right] \\ & + \mathbf{e} \cdot \boldsymbol{\mu} \mathbf{e} \vec{H}_s^i - \frac{\partial \rho \psi}{\partial \vec{\mathbf{H}}^i} \cdot \mathbf{e} \vec{H}_s^i\end{aligned}\tag{70}$$

(71)

C Derivatives for the integration algorithm

$$\frac{\partial R_a^{(k)}}{\partial \alpha_{n+1}} = 1 - \gamma \frac{2}{\vec{M}_c^2} \frac{\partial \bar{\Xi}_{n+1}}{\partial \alpha_{n+1}}\tag{72}$$

$$\frac{\partial R_a^{(k)}}{\partial \gamma} = -\gamma \frac{2 \bar{\Xi}_{n+1}}{\vec{M}_c^2}\tag{73}$$

$$\frac{\partial R_b^{(k)}}{\partial \alpha_{n+1}} = \gamma \frac{2 \bar{\Xi}}{\vec{M}_c^2} \frac{\partial \bar{\Xi}_{n+1}}{\partial \alpha_{n+1}}\tag{74}$$

$$\frac{\partial R_b^{(k)}}{\partial \gamma} = 0\tag{75}$$

D Derivatives for the algorithmic consistent tangent moduli

$$\frac{\partial S}{\partial \alpha} = -\mathbb{C} : \mathbf{I} 2 E_s \alpha + \mathbf{e} \cdot \vec{\mathbf{H}} \quad (76)$$

$$\frac{\partial \vec{\mathbf{B}}}{\partial \alpha} = \mathbf{e}^T : \mathbf{E} - \mathbf{e}^T : \mathbf{I} 3 E_s \alpha^2 + \boldsymbol{\mu} \mathbf{e} \vec{H}_s^i \quad (77)$$

$$\frac{\partial \bar{\Xi}}{\partial \mathbf{E}} = \mathbb{C} : \mathbf{I} 2 \frac{E_s}{\vec{H}_s^i} \alpha - \mathbf{e} \cdot \vec{\mathbf{H}} \frac{1}{\vec{H}_s^i} \quad (78)$$

$$\frac{\partial \bar{\Xi}}{\partial \vec{\mathbf{H}}} = -\mathbf{e}^T : [\mathbf{E} - 3 \mathbf{E}^i] \frac{1}{\vec{H}_s^i} - \boldsymbol{\mu} \mathbf{e} \quad (79)$$

References

- Adly, A., Mayergoz, I., Bergqvist, A., 1991. Preisach modeling of magnetostrictive hysteresis. *Journal of Applied Physics* 69 (8), 5777–5779. [1](#)
- Alexander, P., Brei, D., Miao, W., Halloran, J., Gentilman, R., Schmidt, G., McGuire, P., Hollenbeck, J., 2001. Fabrication and experimental characterization of d₃₁ telescopic piezoelectric actuators. *Journal of Materials Science* 36 (17), 4231–4237. [9.5](#), [9.5](#), [9.5](#), [9.5](#), [24](#)
- Bozorth, R., 1964. Ferromagnetism, 8th Edition. Van Nostrand. [2](#)
- Butz, A., Klinkel, S., Wagner, W., 2008. A piezoelectric 3d-beam finite element formulation accounting for geometrical and material nonlinearities. *International Journal for Numerical Methods in Engineering* DOI:10.1002/nme.2320. [1](#)
- Butz, A., Klinkel, S., Wagner, W., 2005. A nonlinear piezoelectric 3d-beam finite element formulation. In: Bathe, K.-J. (Ed.), *Proceedings Third MIT Conference on Computational Fluid and Solid Mechanics*. Massachusetts Institute of Technology, Cambridge, pp. 291–296. [1](#)
- Calkins, F., Smith, R., Flatau, A., 2000. Energy-based hysteresis model for magnetostrictive transducers. *Magnetics, IEEE Transactions on* 36 (2), 429–439. [1](#)
- Carman, G., Mitrovic, M., 1995. Nonlinear constitutive relations for magnetostrictive materials with applications to 1-d problems. *Journal of Intelligent Material Systems and Structures* 6 (5), 673–683. [1](#)
- Chen, W., Lynch, C., 2001. Multiaxial constitutive behavior of ferroelectric materials. *Journal of Engineering Materials and Technology* 123 (2), 169–175. [1](#)

- Coleman, B., Noll, W., 1963. The thermodynamics of elastic materials with heat conduction and viscosity. *Archive for Rational Mechanics and Analysis* V13 (1), 167–178. [4](#)
- Dapino, M., Flatau, A., Calkins, F., 2006. Statistical analysis of Terfenol-D material properties. *Journal of Intelligent Material Systems and Structures* 17 (7), 587–599. [9.1](#)
- Dapino, M., Smith, R., Calkins, F., Flatau, A., 2002. A coupled magnetomechanical model for magnetostrictive transducers and its application to villari-effect sensors. *Journal of Intelligent Material Systems and Structures* 13 (11), 737–747. [1](#)
- Dapino, M., Smith, R., Faidley, L., Flatau, A., 2000a. A coupled structural-magnetic strain and stress model for magnetostrictive transducers. *Journal of Intelligent Material Systems and Structures* 11 (2), 135–152. [1](#)
- Dapino, M., Smith, R., Flatau, A., 2000b. Structural magnetic strain model for magnetostrictive transducers. *Magnetics, IEEE Transactions on* 36 (3), 545–556. [1](#)
- Elhadrouz, M., Zineb, T., Patoor, E., 2005. Constitutive Law for Ferroelastic and Ferroelectric Piezoceramics. *Journal of Intelligent Material Systems and Structures* 16 (3), 221–236. [1](#)
- Engdahl, G., 2000. *Handbook of Giant Magnetostrictive Materials*. Academic Press, San Diego. [2](#), [9.1](#)
- Fang, D., Feng, X., Hwang, K., 2004. Study of magnetomechanical non-linear deformation of ferromagnetic materials: theory and experiment. *Proceedings of the Institution of Mechanical Engineers Part C-Journal of Mechanical Engineering Science* 218 (12), 1405–1410. [1](#), [3.1](#)
- Huber, J., Fleck, N., 2001. Multi-axial electrical switching of a ferroelectric: theory versus experiment. *Journal of the Mechanics and Physics of Solids* 49 (4), 785–811. [1](#)
- Hwang, S., Huber, J., McMeeking, R., Fleck, N., 1998. The simulation of switching in polycrystalline ferroelectric ceramics. *Journal of Applied Physics* 84 (3), 1530–1540. [1](#)
- Hwang, S., Lynch, C., McMeeking, R., 1995. Ferroelectric/ferroelastic interactions and a polarization switching model. *Acta Metallurgica et Materialia* 43 (5), 2073–2084. [1](#), [9.2](#)
- Ikeda, T., 1990. *Fundamentals of Piezoelectricity*. Oxford University Press. [2](#)
- Jaffe, B., Cook, W., Jaffe, H., 1971. Piezoelectric ceramics. *Acad. Pr.* [2](#)

- Jiles, D., 1995. Theory of the magnetomechanical effect. *Journal of Physics D - Applied Physics* 28 (8), 1537–1546. [1](#)
- Jiles, D., Atherton, D., 1986. Theory of ferromagnetic hysteresis. *Journal of Magnetism and Magnetic Materials* 61 (1-2), 48–60. [1](#)
- Kamlah, M., 2001. Ferroelectric and ferroelastic piezoceramicsmodeling of electromechanical hysteresis phenomena. *Continuum Mechanics and Thermodynamics* 13 (4), 219–268. [1](#), [2](#), [3.1](#), [3.1](#)
- Kamlah, M., Böhle, U., 2001. Finite element analysis of piezoceramic components taking into account ferroelectric hysteresis behavior. *International Journal of Solids and Structures* 38 (4), 605–633. [1](#)
- Klinkel, S., 2006a. A phenomenological constitutive model for ferroelastic and ferroelectric hysteresis effects in ferroelectric ceramics. *International Journal of Solids and Structures* 43 (22-23), 7197–7222. [1](#), [3.2](#)
- Klinkel, S., 2006b. A thermodynamic consistent 1d model for ferroelastic and ferroelectric hysteresis effects in piezoceramics. *Communications in Numerical Methods in Engineering* 22 (7), 727–739. [1](#)
- Landis, C., 2002. Fully coupled, multi-axial, symmetric constitutive laws for polycrystalline ferroelectric ceramics. *Journal of the Mechanics and Physics of Solids* 50 (1), 127–152. [1](#)
- Laskewitz, B., Kamlah, M., Chen, C., 2006. Investigations of the nonlinear behavior of piezoceramic hollow cylinders. *Journal of Intelligent Material Systems and Structures* 17 (6), 521–532. [9.4](#), [9.4](#), [9.4](#), [9.4](#)
- McMeeking, R., Landis, C., 2002. A phenomenological multi-axial constitutive law for switching in polycrystalline ferroelectric ceramics. *International Journal of Engineering Science* 40 (14), 1553–1577. [1](#), [3.1](#), [3.1](#)
- Mehling, V., Tsakmakis, C., Gross, D., 2007. Phenomenological model for the macroscopical material behavior of ferroelectric ceramics. *Journal of the Mechanics and Physics of Solids* 55, 2106–2141. [1](#)
- Moffett, M., Clark, A., Wunfogle, M., Linberg, J., Teter, J., McLaughlin, E., 1991. Characterization of Terfenol-D for magnetostrictive transducers. *Journal of the Acoustical Society of America* 89 (3), 1448–1455. [9.1](#)
- Pasco, Y., Berry, A., 2004. A hybrid analytical/numerical model of piezoelectric stack actuators using a macroscopic nonlinear theory of ferroelectricity and a preisach model of hysteresis. *Journal of Intelligent Material Systems and Structures* 15 (5), 375–386. [1](#)
- Preisach, F., 1935. Über die magnetische nachwirkung. *Zeitschrift für Physik A Hadrons and Nuclei* 94 (5), 277–302. [1](#)

- Sablik, M., Jiles, D., 1993. Coupled magnetoelastic theory of magnetic and magnetostrictive hysteresis. *Magnetics, IEEE Transactions on* 29 (4), 2113–2123. [1](#)
- Schröder, J., Gross, D., 2004. Invariant formulation of the electromechanical enthalpy function of transversely isotropic piezoelectric materials. *Archive of Applied Mechanics* 73 (8), 533–552. [1](#)
- Schröder, J., Romanowski, H., 2005. A thermodynamically consistent mesoscopic model for transversely isotropic ferroelectric ceramics in a coordinate-invariant setting. *Archive of Applied Mechanics* 74 (11-12), 863–877. [1](#), [3.1](#)
- Smith, R., 2005. Smart material systems. Society for Industrial and Applied Mathematics. [1](#), [7](#)
- Smith, R., Dapino, M., Seelecke, S., 2003. Free energy model for hysteresis in magnetostrictive transducers. *Journal of Applied Physics* 93 (1), 458–466. [1](#)
- Tan, X., Baras, J., 2004. Modeling and control of hysteresis in magnetostrictive actuators. *Automatica* 40 (9), 1469–1480. [1](#)
- Taylor, R., 2008. FEAP Manual. <http://www.ce.berkeley.edu/~rlt/feap/>. [9](#)
- Wan, Y., Fang, D., Hwang, K., 2003. Non-linear constitutive relations for magnetostrictive materials. *International Journal of Non-Linear Mechanics* 38 (7), 1053–1065. [1](#)
- Yu, Y., Naganathan, N., Dukkipati, R., 2002a. Preisach modeling of hysteresis for piezoceramic actuator system. *Mechanism and Machine Theory* 37 (1), 49–59. [1](#)
- Yu, Y., Xiao, Z., Naganathan, N., Dukkipati, R., 2002b. Dynamic preisach modelling of hysteresis for the piezoceramic actuator system. *Mechanism and Machine Theory* 37 (1), 75–89. [1](#)
- Zheng, X. J., Sun, L., 2007. A one-dimension coupled hysteresis model for giant magnetostrictive materials. *Journal of Magnetism and Magnetic Materials* 309 (2), 263–271. [1](#)
- Zheng, X., Liu, X., 2005. A nonlinear constitutive model for Terfenol-D rods. *Journal of Applied Physics* 97 (5), 053901. [1](#)